

000 001 PHYSICS-INFORMED CONDITIONAL DIFFUSION FOR 002 MULTI-MODAL PDEs 003 004

005 **Anonymous authors**

006 Paper under double-blind review

007 008 ABSTRACT 009

011 Many physical systems that are represented by partial differential equations
012 (PDEs) admit multiple valid solutions, such as eigenstates of differential operators,
013 or wave modes, yet most neural PDE surrogates are deterministic and col-
014 lapse to averages. This multiplicity of solutions is especially predominant in var-
015 ious engineering and scientific domains ranging from acoustics and seismology
016 to quantum systems. With the ability to generate or complete sparse measure-
017 ments, diffusion-based approaches to solve PDEs by sampling physically valid
018 solutions are gaining traction as an alternative to traditional numerical solvers.
019 In this paper, we present a novel physics-informed conditional diffusion frame-
020 work for multi-modal PDEs, called PDEDIFF, that learns distributions over solu-
021 tion fields from sparse, irregular samples while enforcing governing equations and
022 boundary conditions through mesh-free residual penalties computed by automatic
023 differentiation. PDEDIFF is capable of effectively solving PDEs with multiple
024 valid solutions by learning $\mathbb{P}[Y|X]$, i.e., it learns a solution field Y for a corre-
025 sponding input spatial information X . Unlike Physics-Informed Neural Networks
026 (PINNs), which minimize residuals around expected values $\mathbb{E}[Y|X]$ and hence
027 tend to regress toward a conditional mean, PDEDIFF samples diverse physically
028 consistent solutions by integrating PDE residuals directly into the diffusion objec-
029 tive. Our results indicate that generative, physics-informed diffusion is a practical
030 tool for uncertainty-aware and multi-modal PDE modeling in low-to-moderate di-
031 mensions.

032 1 INTRODUCTION

033 Accurate modeling and solving of partial differential equations (PDEs) is fundamental to advanc-
034 ing scientific disciplines, areas ranging from acoustics and seismology to quantum systems and fluid
035 dynamics. Physics-Informed Neural Networks (PINNs) Raissi et al. (2019a) have emerged as a pow-
036 erful approach for embedding known physical laws into machine learning models. In recent years,
037 PINNs have excelled in incorporating domain-specific equations and information into the learning
038 process by adding residual terms, which include differential equation and boundary conditions, to a
039 regressor’s loss, allowing data-efficient training from limited observations. Despite their ability to
040 leverage domain knowledge and efficiently estimate conditional means ($\mathbb{E}[Y|X]$), PINNs collapse
041 multi-modal target distributions to a single mean-field solution and hence blur distinct physically
042 admissible solutions or eigenstates and fail to capture these multiple scenarios.

043 Diffusion models, driven by advances in deep generative modeling, have achieved remarkable per-
044 formance in tasks requiring detailed sampling from complex probability distributions such as in Ho
045 et al. (2020b); Song et al. (2020). In this paper, we propose using this capability of reversing a noise
046 process to sample from solution fields.

047 Diffusion models have further advanced into multiple domains such as image synthesis Rombach
048 et al. (2022); Kawar et al. (2022); Kakinuma et al. (2025), healthcare Cao et al. (2024); Chung & Ye
049 (2022), and drug discovery Alakhdar et al. (2024); Corso et al. (2023). Conditional variants can, in
050 principle, capture the distribution over solution fields $\mathbb{P}[Y|X]$ rather than a single point estimate, of-
051 fering critical advantages in problems where multiple solutions naturally arise such as parameterized
052 PDEs or in eigen-PDEs. However, standard diffusion models typically do not incorporate physical
053 constraints explicitly, resulting in samples that may violate conservation laws, boundary conditions,
or any other operator constraints.

054 In consideration of the above problems with diffusion models, there are some recent works, like
 055 Basteck et al. (2025) and Shu et al. (2023), that include physics residual as penalties during training.
 056 Yet they targeted cases where the PDE’s solution pairs can be sampled from a single mode distribution.
 057 Also, the above methods retained a grid-based input for training and generation that only
 058 support computation residuals using finite-difference stencils.

059 This ability to sample multiple modes is particularly advantageous in solving PDEs with multiple
 060 solutions, such as Schrodinger equation in quantum mechanics with multiple eigenfunctions Lun-
 061 deen et al. (2011) or multiple wave solutions in Helmholtz equation. Another important setting
 062 where multiple solutions arise is in PDEs with unknown parameters or boundary/initial conditions.
 063 These unknown parameters can either be missing from data recorded during experiments or often
 064 be expensive to measure or reconstruct, thus requiring that solutions from multiple parameter set-
 065 tings be identified that fit the observed measurements. For example, an experimental dataset may
 066 contain records of acoustic waves using multiple sensors in a room, however the source locations
 067 (initial conditions) or room configuration (boundary conditions) for each experiment may not be
 068 fully recorded. In this case, solving the Helmholtz equation to sample multiple solutions that con-
 069 form to the observed sensor readings, while accounting for the physics, would be of interest. In
 070 contrast, standard approaches such as finite difference solvers or even PINNs may either guess a few
 071 parameter values and present solutions for them, or learn a single mean estimated parameter value
 072 across all experiments.

073 Motivated by these challenges, we introduce PDEDIFF, a mesh-free, physics-informed conditional
 074 diffusion framework that learns distributions over solution fields from sparse, irregular samples
 075 while steering generation toward physically valid solutions. The model conditions on coordinates
 076 and uses automatic differentiation to evaluate PDE residuals and boundary or initial conditions di-
 077 rectly at sampled points, therefore no fixed mesh or finite-difference stencils are required. PDED-
 078 IFF’s interface is flexible and compatible with different PDEs and we only replace the residual and
 079 boundary conditions. Therefore, this makes PDEDIFF a complement to classical solvers as these
 080 methods are mesh-specific and equation-specific, whereas our method can be trained once and then
 081 work as a generative surrogate that can produce physics aware solutions at new coordinates without
 082 the need for re-meshing.

083 The key contributions of our work include the following:

- 084 • Generative solver for multi-modal PDEs: PDEDIFF learns distributions over solution fields
 085 and samples distinct, physically admissible modes instead of regressing to an average.
- 086 • Physics-conditioned sampler: A coordinate-conditioned encoder-decoder (CCED) de-
 087 noiser that embeds both spatial coordinates and diffusion time, trained with a dual loss
 088 on data fidelity and residual physics.
- 089 • Mesh-free residual enforcement: Higher-order derivatives are computed via autograd, en-
 090 abling irregular or sparse point clouds rather than fixed grids as used in previous work on
 091 physics-informed diffusion models.
- 092 • Comprehensive evaluations: We benchmark our method on Infinite Potential Wells, Gross-
 093 Pitaevskii Equation, and Helmholtz Equation, reporting the Wasserstein-1 distance and
 094 modality recall against analytical ground truth. We have also experimented on simpler toy
 095 problems with circles similar to the ones in Basteck et al. (2025). Our results indicate that
 096 PDEDIFF outperforms PINNs on PDEs with multiple solutions.

097 2 RELATED WORK

099 2.1 DIFFUSION MODELS

100 With the development of diffusion models Song et al. (2020), Ho et al. (2020b), and Song et al.
 101 (2021), their applications for solving PDEs are emerging. Most of them involve a conditioned
 102 diffusion using score-based method to guide the solution based on sparse observations. Huang
 103 et al. (2024b) proposed training procedure and sampling strategies that are conditioned on incoming
 104 observations to recover accurate PDEs trajectories based on the score-based approach Song et al.
 105 (2021). Qu et al. (2024) consider the inverse problem of data assimilation where they aim to re-
 106 cover the complete weather state from observations of various modalities. Röhling Cachay et al.
 107 (2023) proposed a fully data-driven framework using temporal interpolation as the forward process
 and forecasting as the reverse diffusion process for spatial-temporal forecasting problems. However,

108 relying solely on data-driven approaches may fail to capture the underlying physical laws, potentially leading to samples that lack physical consistency or generalizability beyond the training data.
 109 [Another diffusion-based work Du et al. \(2024\) focus on chaotic systems, but their approach is also](#)
 110 [completely data-driven and implicitly learns the physics distribution with high-fidelity samples.](#)
 111

112 2.2 PHYSICS-INFORMED MODELS

113 PINNs Raissi et al. (2017) have appeared as a robust framework for solving both forward and inverse
 114 problems governed by PDEs. The key idea behind PINNs is to incorporate the PDE directly into
 115 the loss function of a neural network. This is achieved by penalizing the network’s predictions
 116 when they deviate from the physical laws represented by the PDE. As a result, PINNs can learn
 117 solutions even from sparse or noisy training data while ensuring that the learned function respects
 118 the underlying physics. The line of work by Jin et al. (2022) uses feed-forward neural network to
 119 learn the multiple eigenfunctions for the family of Schrödinger’s equations. They achieved multiple
 120 solutions through penalizing with several physics-informed regularizers and iteratively training to
 121 learn new eigenfunctions. However, this approach is only applicable to eigenproblems and would
 122 not be generalized to other types of PDE. Recently, some attention-based methods such as Wu et al.
 123 [\(2024\) use physics-aware attention to learn a deterministic solver on dense meshes and irregular](#)
 124 [geometries, but the learned attention patterns remain unconstrained and may violate fundamental](#)
 125 [physical laws such as boundary conditions, and limiting their reliability.](#)

126 Towards physics informed diffusion-based approaches, CocoGen Jacobsen et al. (2024) [and DiffusionPDE](#)
 127 [Huang et al. \(2024a\) inject](#) the governing equations into the sampling process of score-
 128 based generative models to enforce the consistency of the samples with the underlying PDE, but
 129 physics guidance was only applied to the last N steps. They also focus on the reconstruction prob-
 130 lem that conditioned on grids of sparse measurement. Shysheya et al. (2024) focused on forecasting
 131 tasks with conditioning training and sampling via the score-based approach. Recent works by Bastek
 132 et al. (2025) and Shu et al. (2023) use the Denoising Diffusion Probabilistic Model (DDPM) archi-
 133 tecture combined with physics-informed loss during training. The physics-informed guidance in
 134 Shu et al. (2023) is applied with some probability p_t (a hyperparameter) as an additional input to
 135 the UNET architecture in DDPM. Bastek et al. (2025) models the physics term as a virtual like-
 136 lihood and combines this with the diffusion training loss. Above all, these works employed the
 137 finite difference method to compute the physics-informed guidance. This limited the generalization
 138 of the model as we need to construct the finite difference scheme for every new PDE, which can
 139 become complicated and unstable for high-order derivatives. Also, computing a finite difference
 140 required a fixed grid for consistency. Our work makes use of the automatic differentiation technique
 141 to circumvent these issues.

142 3 BACKGROUND

143 3.1 PARTIAL DIFFERENTIAL EQUATION CONSTRAINTS

144 We consider the following general form for a system of PDEs defined on some domain Ω

$$\begin{cases} \mathcal{F}(u(x)) = f(x), & x \in \Omega \\ \mathcal{B}(u(x)) = b(x), & x \in \partial\Omega \end{cases} \quad (1)$$

145 where \mathcal{F} is the interior differential operator for instance, Laplacian or Hamiltonian, \mathcal{B} encodes the
 146 boundary condition, $\partial\Omega$ is the boundary of domain Ω , and u is the solution field that satisfies the
 147 set of PDEs for all $x \in \Omega$ and boundary conditions $x \in \partial\Omega$. f and b are functions independent
 148 of u , usually representing external conditions applied to the system. In physics-informed learning
 149 setup, along with the data loss, which is the l_2 loss between the generated samples and ground truth
 150 samples, we also aim to minimize a physics residual R . This physics residual is calculated by taking
 151 l_2 difference measuring the extent to which boundary and interior physics constraints are satisfied at
 152 model prediction \hat{u} as given in Raissi et al. (2019b).

$$R(\hat{u}(x), x) = \lambda_{int}\mathcal{L}_\Omega + \lambda_{bc}\mathcal{L}_{bc} \quad (2)$$

$$= \lambda_{int}\|\mathcal{F}(\hat{u}(x)) - f(x)\|_2 + \lambda_{bc}\|\mathcal{B}(\hat{u}(x)) - b(x)\|_2 \quad (3)$$

153 here $\hat{u}(x)$ is the solution predicted by a deep learning model, and \mathcal{L}_{bc} is the physics residual of the
 154 boundary conditions and \mathcal{L}_Ω is the physics residual of PDE constraints defined in the interior of
 155 the domain Ω . λ_{int} and λ_{bc} are the weights that we want to consider for the respective residuals.

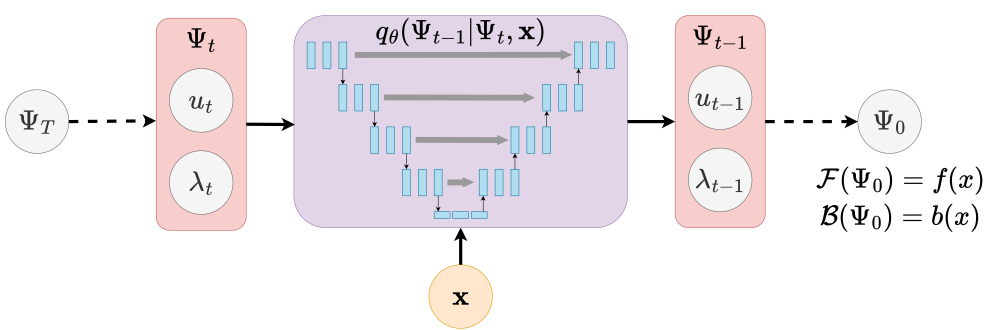


Figure 1: PDEDIFF denoising step denoises random noise into solution field and eigenvalues by conditioning on the spatial coordinates \mathbf{x} . The goal of this coordinate conditioned encoder decoder (CCED) architecture is to generate samples that follow the residual \mathcal{F} and boundary conditions \mathcal{B}

For problems dealing with multiple solutions either through eigen-states or parameterized PDEs, we will be training the generative model to generate both the solution field and eigenvalues/parameters for the differential operators; we revisit this in detail in Section 4.1.

Usually when closed form of a differential operator does not exist, researchers generally opt for a finite difference approach to calculate the derivatives, but this method becomes very unstable for higher order derivatives and that is why we will be using automatic differentiation to eliminate this uncertainty in gradient calculation and making it more flexible than using a grid-based approach.

3.2 DENOISING DIFFUSION PROBABILISTIC MODEL

Diffusion models are a class of deep generative models inspired by non-equilibrium thermodynamics. Ho et al. (2020b) models the forward process by iteratively adding noise to the data so that it resembles a random distribution. Formally, Eq. 4 defines the forward diffusion process, here u_0 is the true data and noise sampled from a gaussian distribution is added over time steps $t \in 1, \dots, T$:

$$p(u_t|u_{t-1}) = \mathcal{N}(u_t; \sqrt{1 - \beta_t}u_{t-1}, \beta_t I), \quad (4)$$

here $\{\beta_t\}_{t=1}^T$ controls the variance schedule in the above equation and after large enough T steps, u_T will resemble a sample from a gaussian distribution. The objective of a diffusion model is to learn a reverse (denoising) process that denoises a sample generated from $\mathcal{N}(0, I)$ into samples from the data distribution p_{data} . Mathematically, the model and the reverse process parameterized by model parameters θ is defined as:

$$q_\theta(u_{t-1}|u_t) = \mathcal{N}(u_{t-1}; \mu_\theta(u_t, t), \Sigma_\theta(u_t, t)), \quad (5)$$

This allows the generation of samples from complex data distributions. In the case of conditional diffusion models, additional information (such as class labels or prompts) is used to condition the denoising network. The model then approximates the full conditional density and generates outputs sampled from the distribution of a desired output class or prompt.

4 METHOD

In this section, we will dive deep into PDEDIFF, a novel conditioned diffusion model framework that learns a distribution corresponding to solution field and parameters in a PDE agnostic setting. We will begin with formalizing the learning task (Sec. 4.1), and derive the physics-informed conditional diffusion algorithm (Sec. 4.1). We will then describe the architecture and the training objective (Sec. 4.2 and Sec. 4.3) and then introduce the metrics used to benchmark the results (Sec. 4.4).

4.1 PROBLEM FORMULATION

Similar to a standard data-driven approach, we will provide the independent variables as input to the diffusion model. The forward and reverse process of the diffusion model then outputs our dependent variables. For our problem setting, we will be working with different PDEs such as Time Independent Schrödinger’s Equation (TISE), and **non-homogeneous** Helmholtz equation. The input for each of the corresponding PDE will be the spatial coordinates x and the output is the corresponding solution field and the parameter that satisfies the PDE. In this paper, we will use $u(x)$ to denote

216 the solution field or eigenfunction and λ to denote the parameter of the differential operator or the
 217 eigenvalue. Both terms will be used interchangeably as we discuss different PDEs.

219 Our method is designed to learn distributions over feasible solutions fields and eigenvalues of the
 220 PDE directly from data. For given spatial coordinates $x \in \Omega \subset \mathbb{R}^d$, the diffusion model is condi-
 221 tioned on x to generate the dependent variables $u(x)$ and λ . The goal of the model is to learn to
 222 generate samples that follow the below PDE:

$$\mathcal{H}_\lambda u(x) = g(x) \quad (6)$$

224 here \mathcal{H}_λ is a [linear or non-linear](#) differential operator (usually of second-order or higher order)
 225 dependent on parameter λ , and $g : \Omega \rightarrow \mathbb{R}$ is a known function, and $u : \Omega \rightarrow \mathbb{R}$ is the solution
 226 field. [The role of \$\lambda\$ in different PDEs works as a system parameter, for instance, in the case of](#)
 227 [eigen-PDEs such as the Schrodinger equation, \$\lambda\$ represents the eigenvalue or the energy of the](#)
 228 [corresponding wavefunction. In the case of the non-homogeneous Helmholtz equation, \$\lambda = k\$ is](#)
 229 [being used to denote the wavenumber that could correspond to different frequencies and waves that](#)
 230 [have been collected from a physical setup. In general form of PDE, \$\lambda\$ will represent the physical](#)
 231 [system parameters such as conductivity, viscosity, Young's Modulus and many more depending on](#)
 232 [the physical system and the PDE describing the system. When PDEDIFF perform sampling, it](#)
 233 [samples the solution field and this system parameter jointly. For simplicity, we only consider PDE](#)
 234 [with Dirichlet boundary condition in our problem formulation, that is, \$\mathcal{B}\(u\(x\)\) = 0\$. But the method](#)
 235 [can be expand to more general setting of any multi-solution PDEs with non-zero boundary condition](#)
 236 [\(Sec. A.5.5\).](#)

237 Given a distribution $p(x)$ where $x \in \Omega$, we are interested in learning the multi-modal condi-
 238 tional density function $p(u(x), \lambda|x)$ from the sparse dataset $\{(x^{(n)}, u^{(n)}, \lambda^{(n)})\}_{n=1}^N$, whose sam-
 239 ples follow the PDEs. For simplicity, we will use $\Psi = (u, \lambda)$ to denote a data point, and
 240 $p(\Psi|x)$ to denote a probability distribution. The forward diffusion process is simulated by gradu-
 241 ally adding controlled Gaussian noise to Ψ , which can be model as a conditional distribution
 242 $p(\Psi_{t+1}(x)|\Psi_t(x), x) \sim \mathcal{N}(\sqrt{1 - \beta_t} \Psi_t(x), \beta_t I)$, where $\{\beta_t\}_{t=1}^T$ is a sequence of noise scheduler.

$$\underbrace{\Psi_T|x}_{\text{Gaussian noise}} \leftarrow \underbrace{\Psi_{T-1}|x}_{\text{Gaussian noise}} \leftarrow \dots \leftarrow \underbrace{\Psi_t|x}_{\text{Gaussian noise}} \leftarrow \dots \leftarrow \underbrace{\Psi_1|x}_{\text{Gaussian noise}} \leftarrow \underbrace{\Psi_0|x}_{\text{real data}}$$

245 This process eventually yields a structured latent representation at timestep T . We adapt the method
 246 from Ho et al. (2020b); Song et al. (2020) to derive a simplified loss function for the denoising
 247 process. Note that the reverse distribution $q(\Psi_t(x)|\Psi_{t+1}(x), x)$ is intractable, we therefore use a
 248 neural network $\text{NN}(\Psi_t, x, t)$ to model the inverse diffusion steps $q_\theta(\Psi_{t-1}|\Psi_t, \Psi_0, x)$ that maximize
 249 the log-likelihood of $q(\Psi_0|x)$:

$$\log q(\Psi_0|x) = \log \int q(\Psi_{0:T}|x) d\Psi_{1:T} \quad (7)$$

250 This log-likelihood is not tractable due to unknown denoising process. Therefore, we will approxi-
 251 mate it with evidence lower bound, which is easier to optimize:

$$\log q(\Psi_0|x) \geq \mathbb{E}_{p(\Psi_{1:T}|\Psi_0, x)} \left[\log \frac{q(\Psi_{0:T}|x)}{p(\Psi_{1:T}|\Psi_0, x)} \right] \quad (8)$$

252 Simplifying the evidence lower bound (further details in the Appendix A.1) gives us

$$\begin{aligned} \log q(\Psi_0|x) &\geq \mathbb{E}_{p(\Psi_1|\Psi_0, x)} \left[\log \frac{q_0(\Psi_0|\Psi_1, x)}{p(\Psi_1|\Psi_0, x)} \right] \\ &\quad + \sum_{t=2}^T \underbrace{\mathbb{E}_{p(\Psi_t|\Psi_0, x)} [D_{KL}(p(\Psi_{t-1}|\Psi_t, \Psi_0, x) || q_\theta(\Psi_{t-1}|\Psi_t, x))]}_{=\mathcal{L}_{\text{data}, t}} \end{aligned} \quad (9)$$

253 In addition to maximizing the likelihood of $q(\Psi_0|x)$, we are also interested in incorporating the
 254 physics guidance in training the diffusion model. Our goal is also to minimize the likelihood of
 255 the residual $q(R(\Psi_0, x)|\Psi_0, x) \sim \mathcal{N}(R(\Psi_0, x), \sigma^2)$, where the variance σ^2 approaches 0 as the
 256 model learns Ψ_0 . In this paper, we consider PDEs of the form $\mathcal{H}_\lambda u(x) = g(x)$. Below is how this
 257 [PDE-loss](#) or $\mathcal{L}_{\text{residual}}$ is defined:

$$\log q(R(\Psi_0, x)|\Psi_0, x) \propto \|\mathcal{H}_\lambda \hat{u}_0 - g\|_2^2 =: \mathcal{L}_{\text{residual}}(\hat{\Psi}_0) \quad (10)$$

270
271**Algorithm 1** PDEDIFF Training

1: **Input:** Training dataset $\Psi_0 = (u_0(x), \lambda_0)$
2: **Output:** Trained denoising process CCED_θ
3: **repeat**
4: $x \sim \text{Uniform}(\Omega)$
5: $\Psi_0(x) \sim q(\Psi_0|x)$ (from training data)
6: $t \sim \text{Uniform}\{1, \dots, T\}$
7: $\epsilon \sim \mathcal{N}(0, I)$
8: $\bar{\alpha}_t = \prod_{s=1}^t (1 - \beta_t)$
9: $\Psi_t(x) = \sqrt{\bar{\alpha}_t} \Psi_0(x) + \sqrt{1 - \bar{\alpha}_t} \epsilon$
10: $\hat{\Psi}_0 = \text{CCED}_\theta(\Psi_t(x), x, t)$
11: Compute $\nabla_\theta \mathcal{L}_{\text{total},t}(\hat{\Psi}_0)$ (as in 11)
12: Update CCED_θ via GD
13: **until** converged

285
286

4.2 TRAINING AND SAMPLING ALGORITHMS

288
289
290
291
292
293
294
295
296
297
298

We follow a similar training objective and approach as given in Ho et al. (2020a); Bastek et al. (2025), where we add a physics informed loss as a regularizer to the entire loss function. The training algorithm in Bastek et al. (2025) uses a finite difference stencil method to calculate the derivatives of the quantities required in the residual. We instead leverage the power of automatic differentiation (autodiff) to calculate the gradients for the residual equations. This strategy provides more flexibility to calculate higher order derivatives as compared to using finite difference stencils, which become unstable when calculating higher order derivatives. Moreover, the finite difference method can only be feasible where the data points are arranged in a regular grid and all the points on the grid correspond to only a single solution, whereas PDEDIFF can train on data points that are randomly sampled from a multi-modal distribution and each generated sample can correspond to any of the feasible solutions.

299
300

We will now introduce the objective function of PDEDIFF that is a loss function composed of the standard reconstruction error and physics informed constraints. The loss function is defined as:

301
302
303

$$\mathcal{L}_{\text{total},t}(\hat{\Psi}_0) = \mathbb{E}_{t \sim [1:T], p(\Psi_{1:T}|x)} \left[c_{\text{data}} \mathcal{L}_{\text{data},t}(\Psi_0, \hat{\Psi}_0) + c_{\text{res}} \mathcal{L}_{\text{residual},t}(\hat{\Psi}_0) \right] \quad (11)$$

where we use it to train a denoising process as in Algorithm 1.

305
306
307
308
309
310
311
312
313
314
315
316
317

Here $\mathcal{L}_{\text{data}}$ is called the data loss which is the reconstruction error between the predicted output and the ground truth values, and for our framework we have used a standard Mean Square Error (MSE) loss. $\mathcal{L}_{\text{residual}}$ is the residual loss, which penalizes the model when the generated samples do not satisfy the underlying physics constraints, i.e., the solutions generated must follow the PDEs. The terms c_{data} and c_{res} are hyperparameters that we set during training to weight the importance of the data loss and physics loss, respectively. Since, we provide the model with the initial spatial and temporal information, we can leverage the use of autodiff to calculate high order derivatives for calculating the residual. This approach also allows us to use randomly sampled data points instead of going with a grid-based approach providing us with more flexibility with respect to the dataset used and also for the sampling part for inference. For PDEDIFF sampling Algorithm 2, we utilize the sampling method from Denoising Diffusion Implicit Model (DDIM) Song et al. (2020) to accelerate the generation process. Also, in step 4 of Algorithm 2, we could replace uniform samples of x_i with any other grid or mesh coordinates for applicable uses.

318
319

4.3 ARCHITECTURE

320
321
322
323

PDEDIFF employs a *coordinate conditioned encoder decoder (CCED)* denoiser that converts a noisy input into its corresponding denoised output by conditioning on the spatial coordinates (independent variable) and diffusion time-step. We pass the noisy input along with the spatial coordinates $x \in \Omega \subseteq \mathbb{R}^d$ and the diffusion time t into the denoiser where each layer is called a *Conditional Block*, which consists of a set of linear and embedding layers. Figure 1 demonstrates how the denois-

Algorithm 2 PDEDIFF Sampling

1: **Input:** Number of samples N , trained denoising process CCED_θ
2: **Output:** Set of samples $\{\Psi_0\}_{i=1}^N$
3: **for** $i = 1$ to N **do**
4: Sample $x_i \sim \text{Uniform}(\Omega)$
5: **for** $t = 1$ to T **do**
6: $\hat{\Psi}_0(x_i) = \text{CCED}_\theta(\Psi_t(x_i), x_i, t)$
7: Sample $\Psi_0(x_i)$ with DDIM Song et al. (2020)
8: **end for**
9: **end for**

Setting	Vanilla		Physics-informed	
	PMSE WD		PMSE WD	
	P	0.822 0.539	1.052	0.344
1D (2 states)	D	0.932 0.157	0.935	0.157
	N	0.809 0.544	0.960	0.446
	Q	0.017 0.086	0.015	0.086
1D (3 states)	P	0.371 0.737	0.460	0.442
	D	0.438 0.114	0.437	0.114
	N	0.333 0.776	0.445	0.470
	Q	0.022 0.055	0.012	0.050
1D GP (3 states)	P	1.550 2.036	1.291	2.418
	D	0.868 1.430	0.867	1.431
	N	0.069 1.180	0.069	1.190
	Q	0.140 0.195	0.126	0.194

Table 1: Performance comparison between PINN (P), DeepONet Lu et al. (2021) (D), Physics-informed Neural Operator Li et al. (2021) (N) and PDEDIFF (Q) across different problem settings for 1D examples. PMSE here is P-MSE and WD is the Wasserstein metric. The lower values represent better match between the ground truth and the sampled wavefunctions. Details of the energy states will be provided in Appendix A.5.1. The first 2 rows correspond to 1D Infinite Potential Well, and 1D GP corresponds to 1D Gross-Pitaevskii Equation.

Setting	Vanilla		Physics-informed		
	PMSE	WD	PMSE	WD	
2D (3 states)	P	1.253	0.378	1.239	0.340
	D	7.327	0.411	7.326	0.410
	N	1.254	0.297	1.398	0.502
	Q	1.222	0.169	1.194	0.156
2D(4 states) degenerate	P	1.250	0.482	1.243	0.477
	D	7.661	0.485	7.659	0.485
	N	1.332	0.299	0.933	0.513
	Q	1.309	0.150	1.338	0.124
2D (4 states) non-degenerate	P	1.133	0.597	1.123	0.623
	D	22.34	0.513	22.34	0.513
	N	1.198	0.344	1.257	0.587
	Q	1.100	0.222	1.091	0.205
Helmholtz Equation	P	0.800	0.107	0.746	0.108
	D	21.35	0.168	21.35	0.168
	N	0.753	0.111	1.000	0.106
	Q	0.253	0.092	0.227	0.091

Table 2: Performance comparison between PINN (P), DeepONet Lu et al. (2021) (D), Physics-informed Neural Operator Li et al. (2021) (N) and PDEDIFF (Q) across different problem settings. PMSE here is P-MSE and WD is the Wasserstein metric. The lower values represent better match between the ground truth and the sampled wavefunctions. Details of the energy states for 2D Schrodinger experiments will be provided in Appendix A.5.3, and of the frequency parameters for the non-homogeneous Helmholtz equation will be provided in Appendix A.5.4.

ing model converts random noise into the corresponding solutions functions and their corresponding eigenvalues or parameters. The details can be found in Appendix A.3.

Further, we use ADAMW for training and we also experiment with different weights for the residual loss (c_{res}) (additional results on this is discussed in Appendix A.8). For baselines, we compare our method with a vanilla conditional diffusion model ($c_{\text{res}} = 0$) with no physics regularization, and we also compare PDEDIFF with a physics-informed fully-connected neural network (PINN) Raissi et al. (2019b), physics-informed neural operator (PINO) Li et al. (2021) and DeepONet Lu et al. (2021). We use the same values of the physics-informed hyperparameter c_{res} for all comparative studies and ablation results. Since for the training algorithm we do not require to implement a custom finite difference stencil and instead proceed with using autodiff, this makes our framework compatible with mesh-free datasets.

4.4 QUANTIFICATION METRICS

Given some spatial input $\mathbf{x} \in \Omega$, PDEDIFF would generate $\Psi_0 = (u_0, \lambda_0)$ corresponding to this \mathbf{x} . The PDEs that it is trying to solve has multiple correct solutions, for e.g., the first 3 wavefunctions and energy values for the Schrödinger’s Equation could correspond to the following possible solutions $(u_0^{(1)}, \lambda_0^{(1)}), (u_0^{(2)}, \lambda_0^{(2)}), (u_0^{(3)}, \lambda_0^{(3)})$. Since each of these is a correct solution to the PDE, we need a metric that can effectively compare the generated samples with the true distribution or the ground truth solutions.

P-MSE: This metric calculates the mean squared error of the samples generated with the ground-truth eigenstates or solutions modes. Formally, the metric can be defined as below:

378

379

$$P\text{-MSE} = \mathbb{E}_{\mathbf{x} \sim \Omega} \left[\left\| \left(\hat{u}_0(\mathbf{x}), \hat{\lambda}_0(\mathbf{x}) \right) - \left(u^{(k(\mathbf{x}))}, \lambda^{(k(\mathbf{x}))} \right) \right\|_2^2 \right] \quad (12)$$

380

381

$$\text{where } k(\mathbf{x}) = \arg \min_{i \in \{1, \dots, M\}} \|\hat{\lambda}_0(\mathbf{x}) - \lambda^{(i)}\|_2 \quad (13)$$

382

383

Here, M is the number of feasible solution modes, $(\hat{u}_0(\mathbf{x}), \hat{\lambda}_0(\mathbf{x}))$ is the generated sample for a particular \mathbf{x} , and $k(\mathbf{x})$ is the function that assigns a particular sample to its closest solution field by comparing the parameter values and this state is then used to calculate the MSE.

384

385

Earth-Mover’s Distance (Wasserstein-1): For two probability measures p, q on a domain $\Omega \subset \mathbb{R}^d$ we use the 1-Wasserstein distance (WD), here $\Gamma(p, q)$ denotes the set of couplings with marginals p and q

386

387

$$W_1(p, q) = \inf_{\gamma \in \Gamma(p, q)} \int_{\Omega \times \Omega} \|\mathbf{x} - \mathbf{y}\| d\gamma(\mathbf{x}, \mathbf{y}), \quad (14)$$

388

389

This metric is used to compare the distances between two probability distributions and in some PDEs, wavefunctions have a special property, i.e., it also represents the probability densities of a particle, i.e., $|\psi|^2$ represents the probability density function of the particle. The ground truth distribution is represented by a linear combination of the probability distribution of the individual solution modes, and the generated distribution can be calculated by squaring the predicted $\psi(\mathbf{x})$.

390

391

To compare the predicted probability distribution and the true distribution, we evaluate both the functions on the same set of point cloud \mathbf{x} . Then the distributions are normalized as below:

392

393

$$p_{\text{pred}}(\mathbf{x}) = \frac{|\psi_{\text{pred}}(\mathbf{x})|^2}{\sum_{\mathbf{x}' \in \mathcal{X}} |\psi_{\text{pred}}(\mathbf{x}')|^2} \quad p_{\text{true}}(\mathbf{x}) = \sum_{i=1}^N \pi_i \frac{|\psi^{(i)}(\mathbf{x})|^2}{\sum_{\mathbf{x}' \in \mathcal{X}} |\psi^{(i)}(\mathbf{x}')|^2} \quad (15)$$

394

395

where $\sum_{i=1}^n \pi_i = 1$ (linear combination coefficients) and after calculating the probability distributions, we use the optimal transport library Flamary et al. (2021).

396

397

5 EXPERIMENT RESULTS

398

399

In this section, we present our experiment setup and results for several PDE problems with multiple solutions such as Time Independent Schrödinger Equation in 1D and 2D infinite potential well, **non-homogeneous** Helmholtz Equation, Gross–Pitaevskii Equation. [More experiment results can be found in Sec. A.5 on some other equations like Burgers’ Equation and toy examples on circle.](#)

400

401

5.1 1D SCHRÖDINGER: PARTICLE IN A BOX

402

403

We consider the time-independent Schrödinger equation for a quantum particle in a one-dimensional infinite potential well:

404

405

$$\underbrace{\left(-\frac{\hbar^2}{2m} \partial_x^2 + V(x) - E \right)}_{\mathcal{H}_E} \psi(x) = 0, \quad V(x) = \begin{cases} 0, & x_L < x < x_R \\ \infty, & \text{otherwise} \end{cases}$$

406

407

where $V(x)$ denotes the infinite potential well, or in other words, the space of a 1D box that contains the particle where it moves freely inside but trapped between the wall (x_L, x_R) defined as above. Note that ∂_x^2 are the second-order derivatives of ψ with respect to x and could be calculate using automatic differentiation to compute the physics informed loss during training. Given this PDE, we are trying to recover the solution field $\psi(x)$ and corresponding energy or parameter E . Results are presented in Table 1 and Figure 2.

408

409

5.2 1D SCHRÖDINGER: GROSS-PITAEVSKII EQUATION

410

411

We consider also one-dimensional time-independent Gross-Pitaevskii equation, a form of non-linear Schrodinger equation. In specific, the Halmiltonian operator \mathcal{H} is non-linear and written as follow:

412

413

414

415

416

417

418

$$\underbrace{\left(\frac{\hbar^2 \partial_x^2}{2m} + V(x) + U_0 |\psi(x)|^2 - E \right)}_{\mathcal{H}_E} \psi(x) = 0$$

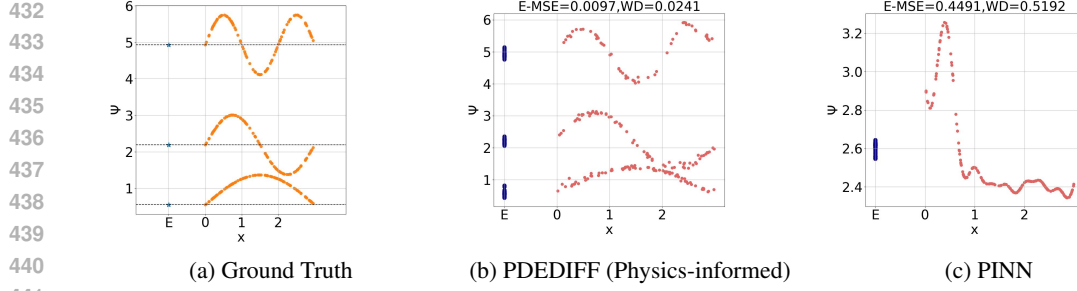


Figure 2: Comparing generated samples by PDEDEIFF and PINN for 1D Schrödinger equation

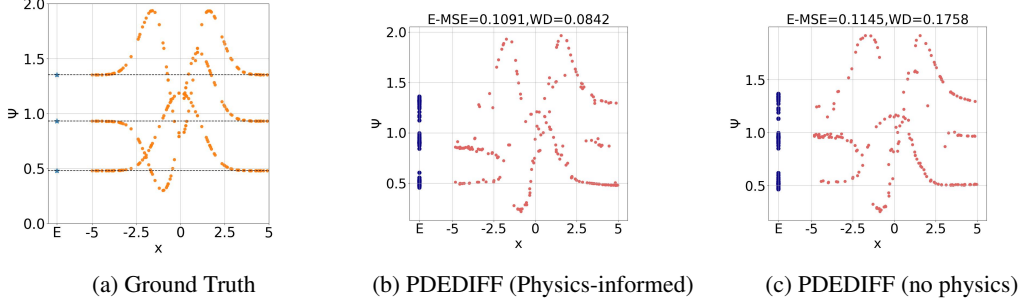
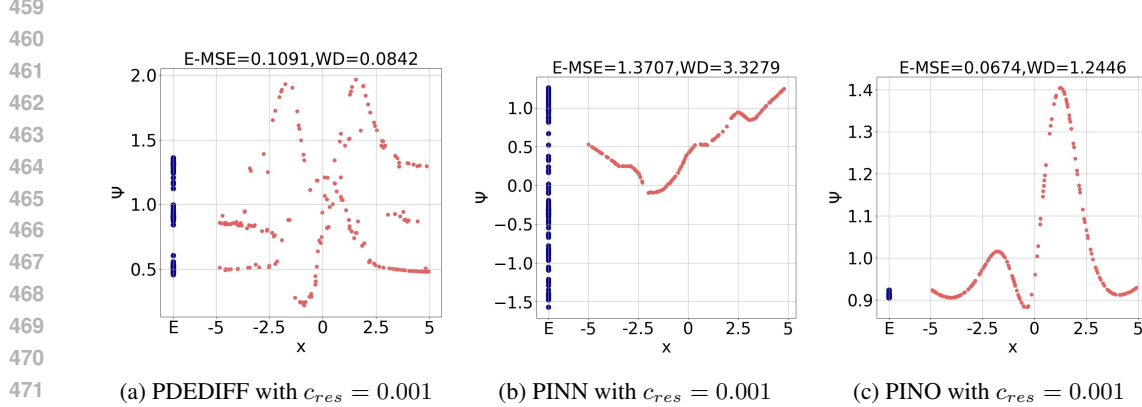


Figure 3: Comparing generated samples by PDEDEIFF for 1D Gross-Pitaevskii equation

455 where U_0 is interaction force, $V(x) = \frac{1}{2}mx^2$ is the harmonic trapping potential. Not many non-
456 linear Schrödinger equations have closed-form solution, such as the one presented here. We obtain
457 training samples and ground truth by solving the time-independent Gross-Pitaevskii equation nu-
458 merically as in Chiofalo et al. (2000). Results are presented in Table 1, Figure 3 and 4.

Figure 4: Generated samples by physics-informed PDEDEIFF, PINN and PINO with $c_{res} = 0.001$ values for 1D Gross-Pitaevskii equation. Although PINO achieves a very low PMSE metric, it collapses to a single mode and results in a high WD metric.

5.3 2D SCHRÖDINGER: PARTICLE IN A BOX

478 We again consider the TISE for a quantum particle in a two-dimensional infinite potential well:

$$\underbrace{\left(-\frac{\hbar^2}{2m}(\partial_x^2 + \partial_y^2) + V(\mathbf{x}) - E \right)}_{\mathcal{H}_E} \psi(\mathbf{x}) = 0, \quad V(\mathbf{x}) = \begin{cases} 0, & x_L < x < x_R, \quad y_L < y < y_R \\ \infty, & \text{otherwise} \end{cases}$$

483 where $\mathbf{x} = (x, y)$ denotes the spatial coordinates and $V(\mathbf{x})$ denotes the 2D infinite potential well. ∂_x^2
484 and ∂_y^2 are the second-order partial derivatives of ψ with respect to x and y . The particle is confined
485 inside the box $\mathbb{B} = [x_L, x_R] \times [y_L, y_R] \subset \mathbb{R}^2$ with Dirichlet boundary conditions, i.e., $\psi(\mathbf{x}) = 0$ for
any $\mathbf{x} \in \partial\mathbb{B}$, where $\partial\mathbb{B}$ denotes the boundary of \mathbb{B} . The results are presented in Tab. 2.

486 5.4 HELMHOLTZ EQUATION
487488 Another case study is the Helmholtz equation that arises from applications in heat conduction or
489 acoustics. The Helmholtz equation is a non-homogeneous elliptic PDE express as follow:

490
$$\underbrace{\nabla^2 \psi(x) + k^2 \psi(x)}_{\mathcal{H}_k \psi} = f(x)$$

491
492

493 where integer or real valued parameter k is known as frequency or wave number, f is a source
494 function that describe the emission source of the wave $\psi(x)$, with $x \in \Omega$. Our goal is to recover
495 the high resolution propagation of the wave through the environment $\psi(x)$ and its frequency k .
496 Training data is simulated by solving the second-order finite-difference linear system $\mathcal{H}_k \psi = f$
497 with low fidelity. The results are presented in Table 2.498 6 DISCUSSION
499500 We observed that PDDEIFF consistently achieves low MSE and WD metric, with physics-informed
501 PDDEIFF achieving the best result in almost all cases (Tab. 1, 2) This demonstrates that PDDEIFF
502 is capable of modeling, generating multimodal distributions and achieves higher numerical accuracy
503 compared to the ground truth. As shown in Fig. 2, PDDEIFF effectively captures the multiple modes
504 present in the training data, while standard feedforward neural networks tend to regress to the mean,
505 failing to represent the distinct modes and instead producing oversmoothed approximations.506 In the case of 1D Schrödinger equation, PDDEIFF has lower errors in both MSE and Wasserstein
507 distance. Incorporating physics-informed guidance further improves performance. Nevertheless,
508 Schrödinger equations have trivial solution where $\psi(x) = 0, E = 0$. This causes problems as with
509 our physics guidance, since the physics loss is also minimized (equal to 0) if the model infers the
510 trivial solution, as observed in our ablation study in A.8, 12 and 13. **For the 1D Gross-Pitaevskii**
511 **equation, PINO achieves a low P-MSE metric but this is due to convergence to a single mode, as**
512 **observed in Fig. 4 and the high WD metric in Tab. 2, while PDDEIFF is able to obtain both low**
513 **P-MSE and WD metric.** We also demonstrate the capabilities of PDDEIFF on 2D Schrödinger
514 equation. In the problem setting of 3 waves, the model is able to learn the different eigenstates
515 and produce samples that are much closer to the true distribution and have a lower MSE loss. In
516 the case where there are 4 waves, the model was trained on both setting wherestates where there
517 are degenerate eigenstates, i.e., 2 eigenstates had the same energy but different wavefunctions, and
518 non-degenerate eigenstates. PDDEIFF is yet able to distinguish the degenerate energy states and
519 generate samples that have a lower Wasserstein metric.520 In inhomogeneous Helmholtz Equation, we tested our framework with 2 parameters. In this setting,
521 we observed that the model picks up the low frequency wave better and it sometimes missed the
522 peak in high frequency wave. **Nevertheless, after training for 5000 epochs, PDDEIFF achieves the**
523 **lowest metric comparing to other baselines, which also trained with the same amount of training**
524 **points and number of epochs (Tab. 2).**

525 7 CONCLUSION

526 We introduced **PDDEIFF**, a physics-informed conditional diffusion framework that samples *entire*
527 *ensembles* of solution fields and eigenvalues for multiple solution PDEs. In contrast, PINNs regress
528 to a conditional mean or collapse to one of the modes. We have also demonstrated that our approach
529 is more flexible than other approaches to incorporating physics in diffusion models in terms of
530 the data samples being mesh-free and also for calculating the physics residuals using automatic
531 differentiation. Also, unlike previous work, we provide the first evidence that physics informed
532 diffusion models can provide better results than physics informed neural networks for PDEs with
533 multiple solutions, and thus are more faithful to the physical law that they must follow. Our work
534 shows a potential towards learning and generating new data for multi-modal PDEs.535 Looking ahead, our framework can potentially be used to explore methods to discover unseen solution
536 fields and eigenvalues that are not observed in data. Similar to recent works, such as Jin et al.
537 (2022), extending PDDEIFF to learning solution fields in a data-free environment is an interesting
538 direction. Scaling this framework to noisy and high-dimensional experimental datasets would enable
539 developing real-time digital simulations of problems that could be studied in much detail and also
accelerate the growth of drug discoveries and sustainable quantum technologies.

540 REFERENCES
541

542 Amira Alakhdar, Barnabas Poczos, and Newell Washburn. Diffusion models in de novo drug design.
543 *Journal of Chemical Information and Modeling*, 64(19):7238–7256, 2024. doi: 10.1021/acs.jcim.
544 4c01107. URL <https://doi.org/10.1021/acs.jcim.4c01107>. PMID: 39322943.

545 Jan-Hendrik Bastek, WaiChing Sun, and Dennis Kochmann. Physics-informed diffusion models.
546 In *The Thirteenth International Conference on Learning Representations*, 2025. URL <https://openreview.net/forum?id=tpYeermigp>.

547

548 Sattik Basu and Sarma L. Rani. Generalized acoustic helmholtz equation and its boundary
549 conditions in a quasi 1-d duct with arbitrary mean properties and mean flow. *Journal of*
550 *Sound and Vibration*, 512:116377, 2021. ISSN 0022-460X. doi: <https://doi.org/10.1016/j.jsv.2021.116377>. URL <https://www.sciencedirect.com/science/article/pii/S0022460X21004296>.

551

552 Chentao Cao, Zhuo-Xu Cui, Yue Wang, Shaonan Liu, Taijin Chen, Hairong Zheng, Dong Liang,
553 and Yanjie Zhu. High-frequency space diffusion model for accelerated mri. *IEEE Transactions*
554 *on Medical Imaging*, 43(5):1853–1865, 2024. doi: 10.1109/TMI.2024.3351702.

555

556 M. L. Chiofalo, S. Succi, and M. P. Tosi. Ground state of trapped interacting bose-einstein condensates by an explicit imaginary-time algorithm. *Phys. Rev. E*, 62:7438–7444, Nov 2000. doi: 10.1103/PhysRevE.62.7438. URL <https://link.aps.org/doi/10.1103/PhysRevE.62.7438>.

557

558 Hyungjin Chung and Jong Chul Ye. Score-based diffusion models for accelerated mri. *Medical Image Analysis*, 80:102479, 2022. ISSN 1361-8415. doi: <https://doi.org/10.1016/j.media.2022.102479>. URL <https://www.sciencedirect.com/science/article/pii/S1361841522001268>.

559

560 Gabriele Corso, Hannes Stärk, Bowen Jing, Regina Barzilay, and Tommi S. Jaakkola. Diffdock:
561 Diffusion steps, twists, and turns for molecular docking. In *The Eleventh International Conference on Learning Representations*, 2023. URL https://openreview.net/forum?id=KKF8_K-mBbS.

562

563 Pan Du, Meet Hemant Parikh, Xiantao Fan, Xin-Yang Liu, and Jian-Xun Wang. Conditional neural
564 field latent diffusion model for generating spatiotemporal turbulence. *Nature Communications*,
565 15(1):10416, November 2024.

566

567 Rémi Flamary, Nicolas Courty, Alexandre Gramfort, Mokhtar Z. Alaya, Aurélie Boisbunon, Stanislas Chambon, Laetitia Chapel, Adrien Corenflos, Kilian Fatras, Nemo Fournier, Léo Gautheron, Nathalie T.H. Gayraud, Hicham Janati, Alain Rakotomamonjy, Ievgen Redko, Antoine Rolet, Antony Schutz, Vivien Seguy, Danica J. Sutherland, Romain Tavenard, Alexander Tong, and Titouan Vayer. Pot: Python optimal transport. *J. Mach. Learn. Res.*, 22(1), January 2021. ISSN 1532-4435.

568

569 Marc Harkonen, Markus Lange-Hegermann, and Bogdan Raita. Gaussian process priors for sys-
570 tems of linear partial differential equations with constant coefficients. In Andreas Krause, Emma
571 Brunskill, Kyunghyun Cho, Barbara Engelhardt, Sivan Sabato, and Jonathan Scarlett (eds.),
572 *Proceedings of the 40th International Conference on Machine Learning*, volume 202 of *Proceedings of Machine Learning Research*, pp. 12587–12615. PMLR, 23–29 Jul 2023. URL
573 <https://proceedings.mlr.press/v202/harkonen23a.html>.

574

575 Jonathan Ho, Ajay Jain, and Pieter Abbeel. Denoising diffusion probabilistic models. *CoRR*,
576 abs/2006.11239, 2020a. URL <https://arxiv.org/abs/2006.11239>.

577

578 Jonathan Ho, Ajay Jain, and Pieter Abbeel. Denoising diffusion probabilistic models. In
579 H. Larochelle, M. Ranzato, R. Hadsell, M.F. Balcan, and H. Lin (eds.), *Advances in Neu-
580 ral Information Processing Systems*, volume 33, pp. 6840–6851. Curran Associates, Inc.,
581 2020b. URL https://proceedings.neurips.cc/paper_files/paper/2020/file/4c5bcfec8584af0d967f1ab10179ca4b-Paper.pdf.

594 Jiahe Huang, Guandao Yang, Zichen Wang, and Jeong Joon Park. DiffusionPDE: Generative
 595 PDE-solving under partial observation. In *The Thirty-eighth Annual Conference on Neural*
 596 *Information Processing Systems*, 2024a. URL <https://openreview.net/forum?id=z0I2SbjN0R>.

598 Jiahe Huang, Guandao Yang, Zichen Wang, and Jeong Joon Park. Diffusionpde: Generative pde-
 599 solving under partial observation, 2024b. URL <https://arxiv.org/abs/2406.17763>.

601 Christian Jacobsen, Yilin Zhuang, and Karthik Duraisamy. Cocogen: Physically-consistent and
 602 conditioned score-based generative models for forward and inverse problems, 2024. URL
 603 <https://arxiv.org/abs/2312.10527>.

604 Henry Jin, Marios Mattheakis, and Pavlos Protopapas. Physics-informed neural networks for quan-
 605 tum eigenvalue problems. In *2022 International Joint Conference on Neural Networks (IJCNN)*,
 606 pp. 1–8, 2022. doi: 10.1109/IJCNN55064.2022.9891944.

608 Yusuke Kakinuma, Takamichi Miyata, Kaito Hosono, and Hirotsugu Kinoshita. Zero-shot image
 609 inpainting using pretrained latent diffusion models. In *2025 International Conference on Artificial*
 610 *Intelligence in Information and Communication (ICAIIC)*, pp. 0803–0807, 2025. doi: 10.1109/
 611 ICAIIC64266.2025.10920775.

612 Bahjat Kawar, Michael Elad, Stefano Ermon, and Jiaming Song. Denoising diffusion restoration
 613 models. In *Proceedings of the 36th International Conference on Neural Information Processing*
 614 *Systems*, NIPS '22. Curran Associates Inc., 2022. ISBN 9781713871088.

615 Zongyi Li, Hongkai Zheng, Nikola B. Kovachki, David Jin, Haoxuan Chen, Burigede Liu, Kamyar
 616 Azizzadenesheli, and Anima Anandkumar. Physics-informed neural operator for learning par-
 617 tial differential equations. *CoRR*, abs/2111.03794, 2021. URL <https://arxiv.org/abs/2111.03794>.

619 Lu Lu, Pengzhan Jin, Guofei Pang, Zhongqiang Zhang, and George Em Karniadakis. Learning
 620 nonlinear operators via DeepONet based on the universal approximation theorem of operators.
 621 *Nature Machine Intelligence*, 3(3):218–229, 2021.

623 Jeff S. Lundeen, Brandon Sutherland, Aabid Patel, Corey Stewart, and Charles Bamber. Direct
 624 measurement of the quantum wavefunction. *Nature*, 474(7350):188–191, 2011. doi: 10.1038/
 625 nature10120.

626 Yongquan Qu, Juan Nathaniel, Shuolin Li, and Pierre Gentine. Deep generative data assimilation in
 627 multimodal setting. 06 2024. doi: 10.1109/CVPRW63382.2024.00050.

629 M. Raissi, P. Perdikaris, and G.E. Karniadakis. Physics-informed neural networks: A deep learning
 630 framework for solving forward and inverse problems involving nonlinear partial differential equa-
 631 tions. *Journal of Computational Physics*, 378:686–707, 2019a. ISSN 0021-9991. doi: <https://doi.org/10.1016/j.jcp.2018.10.045>. URL <https://www.sciencedirect.com/science/article/pii/S0021999118307125>.

634 Maziar Raissi, Paris Perdikaris, and George Em Karniadakis. Physics informed deep learn-
 635 ing (part i): Data-driven solutions of nonlinear partial differential equations. *arXiv preprint*
 636 *arXiv:1711.10561*, 2017.

637 Maziar Raissi, Paris Perdikaris, and George E Karniadakis. Physics-informed neural networks: A
 638 deep learning framework for solving forward and inverse problems involving nonlinear partial
 639 differential equations. *Journal of Computational Physics*, 378:686–707, 2019b.

640 Carl Edward Rasmussen and Christopher K. I. Williams. *Gaussian Processes for Machine Learning*.
 641 The MIT Press, 11 2005. ISBN 9780262256834. doi: 10.7551/mitpress/3206.001.0001. URL
 643 <https://doi.org/10.7551/mitpress/3206.001.0001>.

644 Robin Rombach, Andreas Blattmann, Dominik Lorenz, Patrick Esser, and Bjorn Ommer. High-
 645 Resolution Image Synthesis with Latent Diffusion Models . In *2022 IEEE/CVF Conference on*
 646 *Computer Vision and Pattern Recognition (CVPR)*, pp. 10674–10685, Los Alamitos, CA, USA,
 647 June 2022. IEEE Computer Society. doi: 10.1109/CVPR52688.2022.01042. URL <https://doi.ieee.org/10.1109/CVPR52688.2022.01042>.

648 Salva Röhling Cachay, Bo Zhao, Hailey Joren, and Rose Yu. Dyffusion: A dynamics-
 649 informed diffusion model for spatiotemporal forecasting. In A. Oh, T. Naumann,
 650 A. Globerson, K. Saenko, M. Hardt, and S. Levine (eds.), *Advances in Neural In-*
 651 *formation Processing Systems*, volume 36, pp. 45259–45287. Curran Associates, Inc.,
 652 2023. URL https://proceedings.neurips.cc/paper_files/paper/2023/file/8df90a1440ce782d1f5607b7a38f2531-Paper-Conference.pdf.

654
 655
 656 Dule Shu, Zijie Li, and Amir Barati Farimani. A physics-informed diffusion model for high-fidelity
 657 flow field reconstruction. *Journal of Computational Physics*, 478:111972, April 2023. ISSN
 658 0021-9991. doi: 10.1016/j.jcp.2023.111972. URL <http://dx.doi.org/10.1016/j.jcp.2023.111972>.

660
 661
 662 Aliaksandra Shysheya, Cristiana Diaconu, Federico Bergamin, Paris Perdikaris, José Miguel
 663 Hernández-Lobato, Richard E. Turner, and Emile Mathieu. On conditional diffusion models
 664 for PDE simulations. In *The Thirty-eighth Annual Conference on Neural Information Processing*
 665 *Systems*, 2024. URL <https://openreview.net/forum?id=nQ18EjyMzh>.

666
 667
 668 Jiaming Song, Chenlin Meng, and Stefano Ermon. Denoising diffusion implicit models. *CoRR*,
 669 abs/2010.02502, 2020. URL <https://arxiv.org/abs/2010.02502>.

670
 671
 672 Yang Song, Jascha Sohl-Dickstein, Diederik P Kingma, Abhishek Kumar, Stefano Ermon, and Ben
 673 Poole. Score-based generative modeling through stochastic differential equations. In *Inter-*
 674 *national Conference on Learning Representations*, 2021. URL <https://openreview.net/forum?id=PxTIG12RRHS>.

675
 676
 677 Makoto Takamoto, Timothy Praditia, Raphael Leiteritz, Dan MacKinlay, Francesco Alesiani, Dirk
 678 Pflüger, and Mathias Niepert. PDEBENCH: AN EXTENSIVE BENCHMARK FOR SCI-
 679 EN-TIFIC MACHINE LEARNING. In *ICLR 2023 Workshop on Physics for Machine Learning*, 2023.
 680 URL <https://openreview.net/forum?id=b8Sw0xZQ2kj>.

681
 682
 683 Haixu Wu, Huakun Luo, Haowen Wang, Jianmin Wang, and Mingsheng Long. Transolver: A
 684 fast transformer solver for pdes on general geometries. In *International Conference on Machine*
 685 *Learning*, 2024.

689 A APPENDIX

692 A.1 DERIVATIONS OF SIMPLIFIED TRAINING LOSS

693 Continuing from Sec 4.1 of the main paper, we had briefly discussed the problem formulation of
 694 PDEDIFF. The inverse diffusion step for $q_\theta(\Psi_{t-1}|\Psi_t, \Psi_0, x)$ that maximizes the log-likelihood of
 695 $q(\Psi_0|x)$ is defined in Eq. 7 of the paper as:

$$698 \log q(\Psi_0|x) = \log \int q(\Psi_{0:T}|x) d\Psi_{1:T} \quad (16)$$

700
 701 Below are the steps for deriving and simplifying the lower evidence bound for our conditioned
 DDPM. Note that log of an expectation over a distribution might be intractable, so we consider

702 optimizing the evidence lower bound like previous work Ho et al. (2020b); Song et al. (2020).
 703

$$\begin{aligned}
 704 \log q(\Psi_0|x) &= \log \int q(\Psi_{0:T}|x) d\Psi_{1:T} \\
 705 &= \log \int \frac{q(\Psi_{0:T}|x)}{p(\Psi_{1:T}|\Psi_0, x)} p(\Psi_{1:T}|\Psi_0, x) d\Psi_{1:T} \\
 706 &= \log \mathbb{E}_{p(\Psi_{1:T}|\Psi_0, x)} \left[\frac{q(\Psi_{0:T}|x)}{p(\Psi_{1:T}|\Psi_0, x)} \right] \\
 707 &\geq \mathbb{E}_{p(\Psi_{1:T}|\Psi_0, x)} \left[\log \frac{q(\Psi_{0:T}|x)}{p(\Psi_{1:T}|\Psi_0, x)} \right] \\
 708 &= \mathbb{E}_{p(\Psi_{1:T}|\Psi_0, x)} \left[\log \frac{q(\Psi_T|\Psi_0, x) \prod_{t=1}^T q(\Psi_{t-1}|\Psi_t, x)}{\prod_{t=1}^T p(\Psi_t|\Psi_{t-1}, \Psi_0, x)} \right] \\
 709 &= \mathbb{E}_{p(\Psi_{1:T}|\Psi_0, x)} \left[\log \frac{q(\Psi_T|x) q_0(\Psi_0|\Psi_1, x) \prod_{t=1}^{T-1} q_\theta(\Psi_t|\Psi_{t+1}, x)}{\prod_{t=1}^T p(\Psi_t|\Psi_{t-1}, \Psi_0, x)} \right] \\
 710 &= \mathbb{E}_{p(\Psi_{1:T}|\Psi_0, x)} \left[\log \frac{q(\Psi_T|x) q_0(\Psi_0|\Psi_1, x) \prod_{t=2}^T q_\theta(\Psi_{t-1}|\Psi_t, x)}{\prod_{t=1}^T p(\Psi_t|\Psi_{t-1}, \Psi_0, x)} \right]
 \end{aligned}$$

721
 722 Observed that products inside the log term could be rewritten as
 723

$$\begin{aligned}
 724 \log q(\Psi_0|x) &\geq \mathbb{E}_{p(\Psi_{1:T}|\Psi_0, x)} \left[\log \frac{q(\Psi_T|x) q_0(\Psi_0|\Psi_1, x)}{p(\Psi_1|\Psi_0, x)} + \sum_{t=2}^T \log \frac{q_\theta(\Psi_{t-1}|\Psi_t, x)}{p(\Psi_t|\Psi_{t-1}, \Psi_0, x)} \right] \\
 725 &= \mathbb{E}_{p(\Psi_{1:T}|\Psi_0, x)} \left[\log \frac{q(\Psi_T|x) p_0(\Psi_0|\Psi_1, x)}{p(\Psi_1|\Psi_0, x)} \right] \\
 726 &\quad + \sum_{t=2}^T \mathbb{E}_{p(\Psi_{1:T}|\Psi_0, x)} \left[\log \frac{q_\theta(\Psi_{t-1}|\Psi_t, x)}{p(\Psi_t|\Psi_{t-1}, \Psi_0, x)} \right] \\
 727 &= \mathbb{E}_{p(\Psi_1|\Psi_0, x)} \left[\log \frac{q_0(\Psi_0|\Psi_1, x)}{p(\Psi_1|\Psi_0, x)} \right] + \sum_{t=2}^T \mathbb{E}_{p(\Psi_{t-1}, \Psi_t|\Psi_0, x)} \left[\log \frac{q_\theta(\Psi_{t-1}|\Psi_t)}{p(\Psi_t|\Psi_{t-1}, \Psi_0, x)} \right] \\
 728 &= \mathbb{E}_{p(\Psi_1|\Psi_0, x)} \left[\log \frac{q_0(\Psi_0|\Psi_1, x)}{p(\Psi_1|\Psi_0, x)} \right] \\
 729 &\quad + \sum_{t=2}^T \underbrace{\mathbb{E}_{p(\Psi_t|\Psi_0, x)} [D_{KL}(p(\Psi_{t-1}|\Psi_t, \Psi_0, x) || q_\theta(\Psi_{t-1}|\Psi_t, x))]}_{= \mathcal{L}_{\text{data}, t}}
 \end{aligned}$$

730
 731 A.2 DETAILS OF THE STEPS FOR TRAINING AND SAMPLING ALGORITHM
 732

733 We are also providing details of the training and sampling algorithm here for completeness. The
 734 forward diffusion process is simulated by gradually adding controlled Gaussian noise to Ψ , which
 735 can be model as a conditional distribution $p(\Psi_{t+1}(x)|\Psi_t(x), x) \sim \mathcal{N}(\sqrt{1-\beta_t}\Psi_t(x), \beta_t I)$, where
 736 $\{\beta_t\}_{t=1}^T$ is a sequence of noise scheduler.
 737

738 A.2.1 LATENT STEPS FOR TRAINING
 739

740 We can use reparametrization trick to write $p(\Psi_{t+1}(x)|\Psi_t(x), x)$ as
 741

$$\Psi_{t+1}(x) = \sqrt{1-\beta_t}\Psi_t(x) + \sqrt{\beta_t}\epsilon_t, \quad \epsilon_t \sim \mathcal{N}(0, I)$$

742 We can unroll Ψ_{t+1} based on Ψ_{t-1}
 743

$$\begin{aligned}
 744 \Psi_{t+1}(x) &= \sqrt{1-\beta_t}(\sqrt{1-\beta_{t-1}}\Psi_{t-1}(x) + \sqrt{\beta_{t-1}}\epsilon_{t-1}) + \sqrt{\beta_t}\epsilon_t, \quad \epsilon_{t-1} \sim \mathcal{N}(0, I) \\
 745 &= \sqrt{1-\beta_t}\sqrt{1-\beta_{t-1}}\Psi_{t-1}(x) + \sqrt{1-\beta_t}\sqrt{\beta_{t-1}}\epsilon_{t-1} + \sqrt{\beta_t}\epsilon_t \\
 746 &= \sqrt{1-\beta_t}\sqrt{1-\beta_{t-1}}\Psi_{t-1}(x) + \sqrt{1-(1-\beta_t)(1-\beta_{t-1})}\epsilon
 \end{aligned}$$

756 where $\epsilon \sim \mathcal{N}(0, I)$; and the third equal sign holds since sum of two Gaussian distribution is also a
 757 Gaussian distribution.

758 Unroll with respect to t , we have Ψ_{t+1} in term of Ψ_0

$$\begin{aligned} 760 \quad \Psi_{t+1}(x) &= \sqrt{1 - \beta_t} \sqrt{1 - \beta_{t-1}} \Psi_{t-1}(x) + \sqrt{1 - (1 - \beta_t)(1 - \beta_{t-1})} \epsilon \\ 761 \\ 762 \quad &= \prod_{s=1}^{t+1} \sqrt{1 - \beta_s} \Psi_0(x) + \sqrt{1 - \prod_{s=1}^{t+1} (1 - \beta_s)} \epsilon \\ 763 \\ 764 \end{aligned}$$

765 So for brevity of notation, we denote

$$766 \quad \bar{\alpha}_{t+1} = \prod_{s=1}^{t+1} (1 - \beta_s) \quad (17) \\ 767 \\ 768$$

769 as used in Algorithm 1 of the main paper.

771 A.2.2 DDIM SAMPLING

773 We adapt the sampling technique from Song et al. (2020) for more efficient sampling. Details are
 774 provided here for completeness.

775 In step 6 of Algorithm 2, we obtain

$$777 \quad \hat{\Psi}_0(x_i) = \text{CCED}_\theta(\Psi_t(x_i), x_i, t) \quad (18) \\ 778$$

779 We can update denoise step $\Psi_{t-1}(x_i)$ using the predicted $\hat{\Psi}_0(x_i)$ and $\Psi_t(x_i)$

$$780 \quad \Psi_{t-1}(x_i) = \sqrt{\bar{\alpha}_{t-1}} \hat{\Psi}_0(x_i) + \sqrt{\frac{1 - \bar{\alpha}_{t-1}}{1 - \bar{\alpha}_t}} \left(\Psi_t(x_i) - \sqrt{\bar{\alpha}_t} \hat{\Psi}_0(x_i) \right) \quad (19) \\ 781 \\ 782$$

783 with $\bar{\alpha}_t$ defined as in A.2.1.

784 A.3 ARCHITECTURE IMPLEMENTATION

786 In Sec. 4.3 of the main paper, we had briefly discussed that PDEDIFF employs a coordinate-
 787 conditioned encoder decoder (CCED) denoiser that converts a noisy input into its corresponding
 788 denoised output by conditioning on the spatial coordinates.

789 The first step in the CCED forward pass is the encoder, where the noisy input, \mathbf{x} and t are passed
 790 through this encoder layer that has multiple sets of the *Conditional Block* and between each of these
 791 blocks, the activation function used is *softplus* or *tanh* based on the problem setting and the residual
 792 equations involved. This encoder converts all this data into a low-dimensional latent representation.

794 The next step is the bottleneck layer that also consists of the *Conditional Block* and captures the en-
 795 coding within this low dimensional latent space to capture critical information required for denoising
 796 the input.

797 After the bottleneck layer, the latent information passes through the decoder, similar to the encoder,
 798 transforms the latent information into the original domain to give us the predicted noise. Every layer
 799 of this decoder also has a skip connection from the encoder layer to effectively relay the encodings
 800 to improve efficiency and accuracy.

801 We implement PDEDIFF in PyTorch 2.5.1 with CUDA 12.0 on an NVIDIA A100
 802 GPU. All random seeds were fixed using `torch.manual_seed`, `np.random.seed`, and
 803 `torch.cuda.manual_seed`.

804 We use a lightweight CCED to predict $(\hat{\psi}, \hat{E})$ given noisy input \mathbf{z} , the diffusion timestep $t \in$
 805 $\{0, \dots, T-1\}$, and the spatial coordinate \mathbf{x} :

806 Diffusion Hyperparameters:

- 808 • *Steps*: $T = 100$.
- 809 • *Noise schedule*: cosine, $\beta_t \in [10^{-5}, 10^{-2}]$

- *Objective*: DDPM L_{simple} on x_0 plus physics residual weight c_{res}
- *Optimizer*: AdamW, lr = 5×10^{-4}
- *Training*: 1000 updates, batch 32
- *Sampling*: deterministic DDIM “single-step”

The implementation of our code can be found at: code

A.4 METRICS FOR TOY EXAMPLES

We discussed the P-MSE and Wasserstein metric for Schrodinger equations. For toy examples where we consider settings involve circles, the metrics are defined slightly different from that of the ones described in Section 4.4 of the main paper since we do not have explicit eigenvalues for circle setups, and distributions on circles are not similar to those belongs to wavefunctions. We used mean squared error (MSE) to and Wasserstein distance on uniform distribution of circles (setting dependent) to evaluate the generated samples against ground truth values.

A.4.1 MEAN SQUARED ERROR

This metric calculates the mean squared error of the samples generated with the ground truth circles coordinates. We compute the squared distance to all possible y -coordinates for an spatial x and simply choose the minimum. Formally, the metric can be defined as below:

$$\text{MSE} = \mathbb{E}_{\mathbf{x} \sim \Omega} \left[\min_{y_i \in \mathcal{Y}} \|\hat{y} - y_i\|_2^2 \right]$$

where \mathcal{Y} is set of possible solution of y -coordinates

A.4.2 WASSERSTEIN DISTANCE ON UNIFORM DISTRIBUTIONS

For two probability measures p, q on a domain $\Omega \subset \mathbb{R}^d$ Denotes $\Gamma(p, q)$ the set of couplings with marginals p and q

$$W_1(p, q) = \inf_{\gamma \in \Gamma(p, q)} \int_{\Omega \times \Omega} \|\mathbf{x} - \mathbf{y}\| \, d\gamma(\mathbf{x}, \mathbf{y}), \quad (20)$$

where $\Gamma(p, q)$ denotes the set of couplings with marginals p and q .

Let $\{x_i\}_{i=1}^n \subset \mathbb{R}$ denote sampled x -coordinates and let $\{\hat{y}_i\}_{i=1}^n$ be the predicted y -values from a model. We define a uniform distribution on (x_i, \hat{y}_i) pairs. We define the predicted distribution to be

$$p_{\text{pred}}((x_i, \hat{y}_i)) = \frac{1}{n} \delta_{(x_i, \hat{y}_i)}$$

Unit circle. We define the distribution for ground truth pairs (x_i, y_i) for each x_i uniformly sampled from $[-1, 1]$ as follow

$$p_{\text{true}}((x_i, y_i)) = \frac{1}{2n} \delta_{(x_i, y_i)}, \quad \text{where } \delta_{(x_i, y_i)} = \begin{cases} 1, & \text{if } x_i^2 + y_i^2 = 1 \\ 0, & \text{otherwise} \end{cases}$$

Disjoint circles We define the distribution for ground truth pairs (x_i, y_i) for each x_i uniformly sampled from $[-1, 3]$ as follow

$$p_{\text{true}}((x_i, y_i)) = \sum_{k=1}^2 \pi_k \frac{1}{2n} \delta_{(x_i, y_i)}$$

where

$$\delta_{(x_i, y_i)} = \begin{cases} 1, & \text{if } x_i^2 + y_i^2 = 1, x_i < 1 \text{ or } (x_i - 2)^2 + (y_i - 2)^2 = 1, x_i \geq 1 \\ 0, & \text{otherwise} \end{cases}$$

864 and π_k is the weight if (x_i, y_i) belongs to circle k ($k = 1$ for circle centers at $(0, 0)$ and $k = 2$ for
 865 circle centers at $(2, 2)$)

866 **Concentric circles** We define the distribution for ground truth pairs (x_i, y_i) for each x_i uniformly
 867 sampled from $[-1, 1]$ as follow

$$869 \quad p_{\text{true}}((x_i, y_i)) = \sum_{k=1}^2 \pi_k \frac{1}{2kn} \delta_{(x_i, y_i)}$$

$$870$$

$$871$$

872 where

$$873 \quad \delta_{(x_i, y_i)} = \begin{cases} 1, & \text{if } (x_i, y_i) \in \mathcal{C} \\ 0, & \text{otherwise} \end{cases}$$

$$874$$

$$875$$

876 with

$$877 \quad \mathcal{C} = \mathcal{C}_1 \cup \mathcal{C}_2$$

$$878 \quad \text{with } \mathcal{C}_1 = \{(x_i, y_i) : x_i^2 + y_i^2 = 9, \text{ and } x_i \notin [-1, 1]\}$$

$$879$$

$$880 \quad \mathcal{C}_2 = \{(x_i, y_i) : x_i^2 + y_i^2 = 1 \text{ or } x_i^2 + y_i^2 = 9, \text{ and } x_i \in [-1, 1]\}$$

$$881$$

882 and π_k is the weight if (x_i, y_i) belongs to \mathcal{C}_k .

884 A.5 EXPERIMENT SETUP

885 In this section, we continue from Section 5 of the main paper and discuss the results of PDDEIFF in
 886 the problem settings defined earlier. We first discuss more details of the problem settings, i.e. how
 887 did we generate data for training and hyperparameters used in each physics setting.

889 A.5.1 1DSCHRODINGER: INFINITE POTENTIAL WELL/ PARTICLE IN A BOX

890 We consider the time-independent Schrödinger equation for a particle in a one-dimensional infinite
 891 potential well:

$$894 \quad E\psi(x) = \underbrace{\left(-\frac{\hbar^2}{2m} \partial_x^2 + V(x) \right)}_H \psi(x)$$

$$895$$

$$896$$

$$897$$

898 where $V(x)$ denotes the infinite potential well, or in other words, the space of a 1D box that contains
 899 the particle where it moves freely inside but trapped between the wall (x_L, x_R) . The potential well
 900 can be defined as

$$902 \quad V(x) = \begin{cases} 0, & x_L < x < x_R \\ \infty, & \text{otherwise} \end{cases}$$

$$903$$

$$904$$

905 In this setting, the particle is confined within (x_L, x_R) , with Dirichlet boundary conditions $\psi(x_L) =$
 906 $\psi(x_R) = 0$.

907 Solving for $\psi(x)$, we can do it analytically as outside of x_L, x_R , $\psi(x) = 0$, so the wavefunction
 908 takes the form:

$$910 \quad \psi(x) = \sqrt{\frac{2}{L}} \sin\left(\frac{n\pi x}{L}\right)$$

$$911$$

912 where n are positive integer values.

913 **Dataset Generation:** The dataset for 1D infinite potential well was generated by uniformly sampling
 914 spatial coordinates between $[0, L_x]$. After sampling the spatial coordinates, we analytically calculate
 915 the wavefunction and the energy values. For our experiments, we simplify the constant values as
 916 $\hbar = 1$, $m = 1$, and the size of the well is taken as $L_x = 3$. We generate 100 data points for each of
 917 the first few eigenstates for training, i.e. we choose $n = 1, 2, 3$ for the 1D TISE 3 waves setting, and
 $n = 1, 2$ for the 1D TISE 2 waves setting.

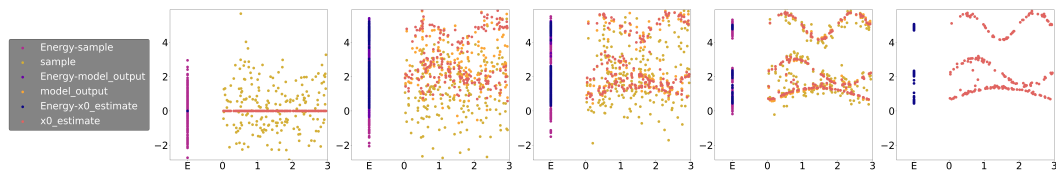


Figure 5: PDEDIFF denoising steps with $c_{res} = 0.001$ (left to right: denoise step $t = 100, 70, 40, 10, 0$). The left-most subplot shows noisy samples from Gaussian and each of the steps to the right shows the denoising process. The right-most subplot show the generated samples Ψ_0 .

A.5.2 1D GROSS-PITAEVSKII EQUATION

We consider also one-dimensional time-independent Gross-Pitaevskii equation, a form of non-linear Schrodinger equation. In specific, the Halmiltonian operator \mathcal{H} is non-linear and written as follow:

$$E\psi(x) = \underbrace{\left(\frac{\hbar^2 \partial_x^2}{2m} + V(x) + U_0 |\psi(x)|^2 \right)}_{\mathcal{H}} \psi(x)$$

where U_0 is interaction force, $V(x) = \frac{1}{2}mx^2$ is the harmonic trapping potential.

Not many non-linear Schodinger equations have closed-form solution, such as the one presented here. We obtain training samples and ground truth by solving the time-independent Gross-Pitaevskii equation via an explicit imaginary-time algorithm as in Chiofalo et al. (2000).

Setup: In this setting, the particle is free to move within $(x_L, x_R) \subset \mathbb{R}$, with Dirichlet boundary conditions $\psi(x_L) = \psi(x_R) = 0$. We generate 100 data points for each wavefunction and their corresponding energy using the algorithm in Chiofalo et al. (2000) for training and generate 200 points to evaluate our framework against the ground truth.

A.5.3 2DSCHRODINGER: SQUARE INFINITE POTENTIAL WELL

We next consider the time-independent Schrödinger equation for a particle in a two-dimensional square infinite potential well:

$$E\psi(\mathbf{x}) = \underbrace{\left(-\frac{\hbar^2}{2m}(\partial_x^2 + \partial_y^2) + V(\mathbf{x}) \right)}_{\mathcal{H}} \psi(\mathbf{x})$$

where $V(\mathbf{x})$ denotes the infinite potential well, or in other words, the space of a 2D box that contains the particle where it moves freely inside but trapped between the walls $\mathbb{B} = [x_L, x_R] \times [y_L, y_R] \subset \mathbb{R}^2$. The potential well can be defined as:

$$V(\mathbf{x}) = \begin{cases} 0, & x_L < x < x_R, \quad y_L < y < y_R \\ \infty, & \text{otherwise} \end{cases}$$

In this setting, the particle is confined within \mathbb{B} , with Dirichlet boundary conditions, i.e., $\psi(\mathbf{x}) = 0$ for any $\mathbf{x} \in \partial\mathbb{B}$, where $\partial\mathbb{B}$ denotes the boundary of the box \mathbb{B} .

Solving for $\psi(\mathbf{x})$, we can do it analytically as outside of \mathbb{B} , $\psi(\mathbf{x}) = 0$, so the wavefunction takes the form:

$$\psi(\mathbf{x}) = \frac{2}{L} \sin\left(\frac{n_x \pi x}{L}\right) \sin\left(\frac{n_y \pi y}{L}\right)$$

where n_x, n_y are positive integer values.

Set up: The dataset for 2D infinite potential well was generated by uniformly sampling spatial co-ordinates between $x = [0, L_x]$, $y = [0, L_y]$. After sampling the spatial coordinates, we analytically

972 calculate the wavefunction and the energy values. For our experiments, we simplify the constant
 973 values as $\hbar = 1, m = 1$, and the size of the well is taken as $L_x = L_y = 3$. For each eigen-
 974 state, we sample 200 data points for all the states in total. For 3 wave setting, we choose the states
 975 (n_x, n_y) as $(1, 1), (2, 1), (2, 2)$, and for the 4 wave settings, we experiment on degenerate states
 976 $(1, 1), (1, 2), (2, 1), (2, 2)$, i.e. some wavefunctions has the same energy, and nondegenerate states
 977 $(1, 1), (2, 1), (3, 1), (4, 1)$, i.e. every wavefunctions has distinct energy.

978

979

A.5.4 HELMHOLTZ EQUATION

980 The Helmholtz equation is a non-homogeneous elliptic PDE that usually arises from applications in
 981 heat conduction, ultrasound or acoustics Basu & Rani (2021). It can be express as follow:

$$982 \underbrace{\nabla^2 \psi(x) + k^2 \psi(x)}_{\mathcal{H}_k \psi} = f(x)$$

$$983$$

$$984$$

985 where the integer or real valued parameter k is known as frequency or wave number, and the source
 986 function f describes the emission source of the wave $\psi(x)$, with $x = (x_1, x_2) \in \Omega \subseteq \mathbb{R}^2$. In our
 987 experiment, we use the following source function

$$988 f(x) = (1 + 8\pi^2) \cos(\pi^2 x_1) \cos(\pi^2 x_2)$$

989 Our goal is to recover the high resolution propagation of the wave through the environment $\psi(x)$
 990 and its frequency k . Training data is simulated by solving the second-order finite-difference linear
 991 system $\mathcal{H}\psi = f$ with low fidelity on a 16×16 grid. The results are presented in Tab. 2 and 11.

992

Setup: We sample 128 data points for each wave mode from a 16×16 grid and their corresponding
 993 frequency $k \in \{\pi, 4\pi\}$. The ground truth solution grids for training and evaluating our framework
 994 against the ground truth are obtained using the linear algebra solver on the discrete differential operator
 995 by second-order finite differences. Since only ground truth on fixed grid can be obtain through
 996 numerical method, we sample from fixed grid points for evaluation as in figure 6c, comparing against
 997 the ground truth in figure 6a and the prediction via PINN in figure 6b. In practical use cases, we can
 998 sample from any possible partial coordinate to complete the solution space via sampling from the
 999 learned PDEDIFF model, and hence can obtain multiple higher resolution solution fields on 32×32
 1000 grid with this method such as in figure 6d. The accuracy of the generated sample can be observed
 1001 from slices of the 2D solution as in figures 6e-f for better visualization.

1002

1003

A.5.5 BURGERS' EQUATION

1004 We consider the 1D viscous Burgers' equation, a nonlinear PDE widely used as a simplified model
 1005 of Navier-Stokes equations. In a more practical setting, we consider measurements of fluid dynamics
 1006 with various viscosity. Assume that measurements of the fluid flow and viscosity are difficult and
 1007 only low-fidelity, sparse measurements are obtained, and some governed physics are known in the
 1008 form of the viscous Burger's equation Takamoto et al. (2023)

$$1009 \partial_t u(t, x) + \frac{1}{2} \partial_x u^2(t, x) = \nu \partial_{xx} u(x, t), \quad x \in (0, 1), t \in (0, 2]$$

$$1010$$

$$1011 u(0, x) = u_0(x), \quad x \in (0, 1)$$

1012 where $u(t, x)$ denotes the flow velocity and ν is the viscosity controlling smoothness of the solution
 1013 and a periodic boundary condition.

1014

Setup: We utilize the 1D Burgers' Equation dataset from PDEBench Takamoto et al. (2023). To
 1015 simulate a scenario where governed physics are known but measurements are sparse, we isolate a
 1016 fixed initial condition trajectory and observe its evolution under varying physical parameters. We
 1017 extract solution fields for $\nu \in \{0.001, 0.4\}$ and subsample from the original high-resolution data.
 1018 For training, we generate a dataset by uniformly sampling 100 spatial coordinate points for each
 1019 (viscosity, time) pair, resulting in a sparse representation of the fluid flow across the spatiotemporal
 1020 domain.

1021

1022

A.5.6 TOY EXAMPLES

1023

1024 In this section, we discuss in more details for the experiment setup for the toy examples with circles.
 1025 Given some x coordinates that are uniformly sampled from a given range (such as $[-1, 1]$ for unit
 circle). We want to generate the corresponding y coordinates that satisfy physics guidance.

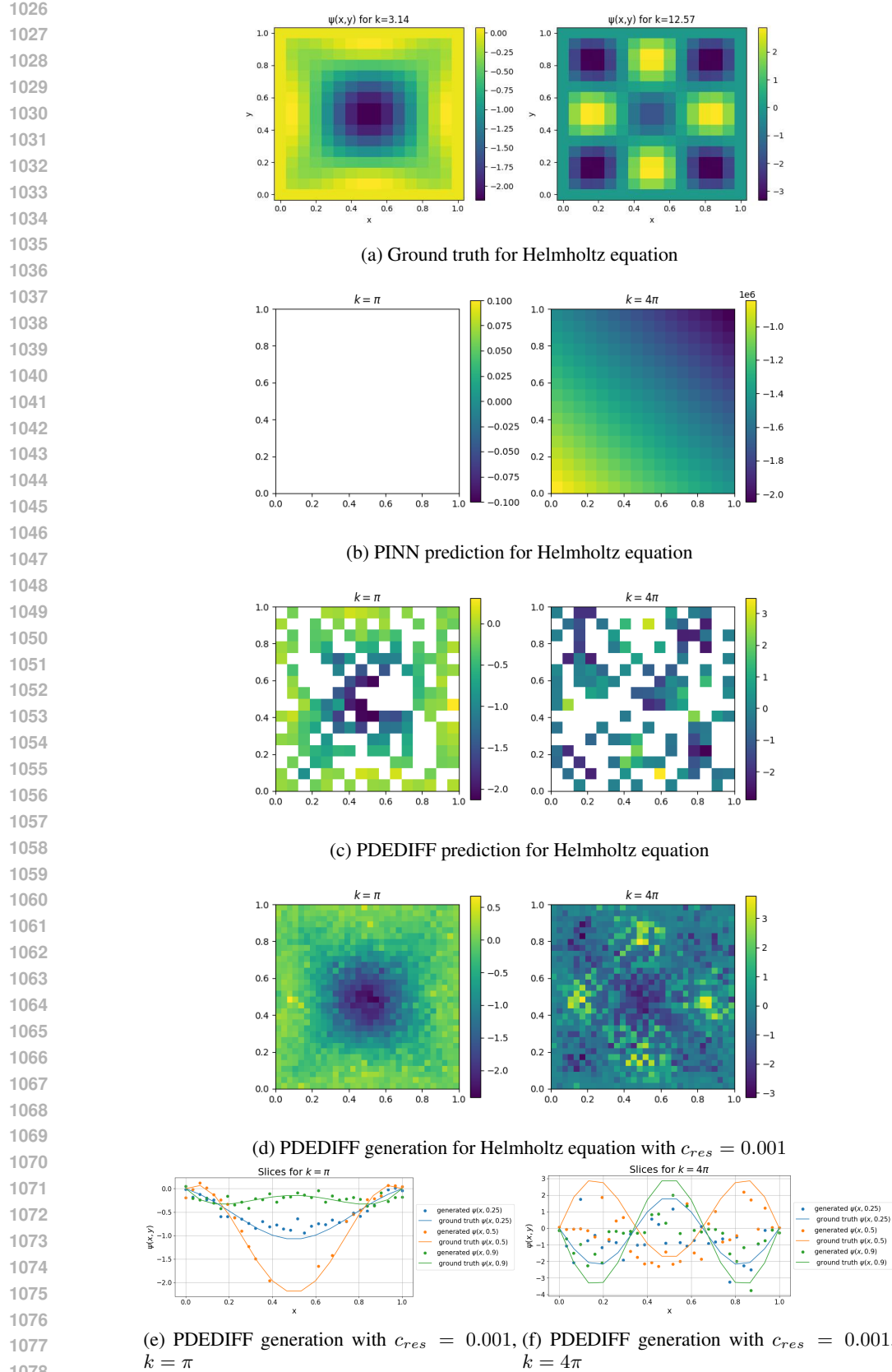


Figure 6: Ground truth, prediction by PINN and generated samples by physics-informed PDDEIFF

Setting	Burgers Equation	
	P	Q
0	0.0516 ± 0.0024	0.0149 ± 0.0025
0.001	0.0685 ± 0.0119	0.0148 ± 0.0023
0.005	0.0956 ± 0.0019	0.0199 ± 0.0026
0.01	0.1043 ± 0.0045	0.0233 ± 0.0039
0.05	0.1200 ± 0.0009	0.0375 ± 0.0084
0.1	0.1220 ± 0.0007	0.0406 ± 0.0079
0.5	0.1283 ± 0.0004	0.0496 ± 0.0102
1	0.1301 ± 0.0028	0.0540 ± 0.0106
10	0.1264 ± 0.0137	0.0710 ± 0.0101
100	0.1063 ± 0.0494	0.0782 ± 0.0122

Table 3: Preliminary performance comparison between PINN (P) and PDEDIFF (Q) for Burger’s Equation for a particular trajectory with 2 different viscosities over the entire space and time values on P-MSE metric. The lower values represent better match between the ground truth and the sampled datapoints.

Unit circle. This problem could be formulated as a simple problem $\sqrt{1 - x^2} = \pm y$, in which the “eigen-values” ± 1 is not explicitly exposed to the model. We instead required the model to learn this and output $y|x$ from provided training pairs (x, y) and the physical constraints $x^2 + y^2 = 1$. Note that for a given x , there are 2 possible values for y —coordinates. We generate 100 points on the unit circle with coordinates (x, y) satisfying $x^2 + y^2 = 1$ for training.

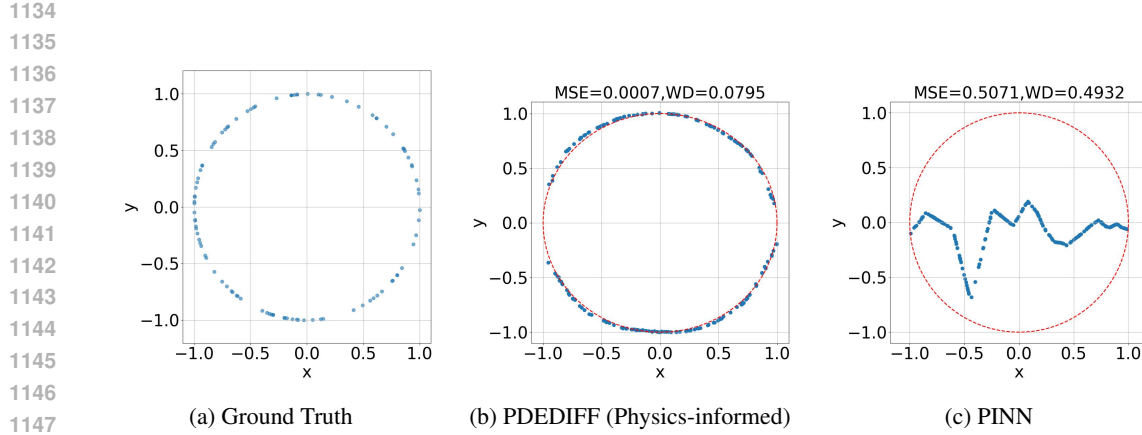
Disjoint circle. To study if the diffusion model is able to learn distinct distributions, we generate 200 points, with 100 points on a unit circle with coordinates (x, y) satisfying $x^2 + y^2 = 1$ with centroid at $(0, 0)$, and another 100 points on a circle with coordinates (x, y) satisfying $(x-2)^2 + (y-2)^2 = 1$ with center at $(2, 2)$. The two circles do not overlap each other.

Concentric circle. We generate 200 points, with 100 points on a circle with coordinates (x, y) satisfying $x^2 + y^2 = 1$, and another 100 on a circle with coordinates (x, y) satisfying $x^2 + y^2 = 9$. The two circles share the same centroid at $(0, 0)$. This creates a more complicated setting where for some x coordinates, there exist 4 possible solutions. Figure 9 illustrates that PDEDIFF manages to distinguish different distributions, while PINN collapsed to only learning the mean of the data.

For circle settings, we consider the weighting for physics informed loss $c_{res} = 0.01$. To obtain new samples for visualization and error quantification, we generate 200 points with Algorithm 2 of the main paper. The generation by physics-informed PDEDIFF with $c_{res} = 0.01$ can be visualize at figures 7b, 8b, 9b for unit circle, disjoint circles and concentric circles, respectively. In comparison, generation by PINN (also with $c_{res} = 0.01$) are shown in Figures 7c, 8c, 9c, for unit circle, disjoint circles and concentric circles, respectively. For each toy setting, we run 5 experiments for each models on different seeds and present the average and one standard deviation of the metrics obtained with each model in table 4. In general, the performance of PDEDIFF with physics-informed loss outperforms that of PINN with similar residual coefficient c_{res} , assessed using the P-MSE and the Wasserstein metric. The experiments with toy examples of circles verify the performance of our method and show potential of physics-informed diffusion in distinguishing multimode distribution.

A.6 COMPARISON WITH GAUSSIAN PROCESSES

We have performed a small set of experiments to compare PDEDIFF with Gaussian Processes as in Rasmussen & Williams (2005). These methods discuss how the differential operator could be embedded into the gaussian prior ensuring that the samples generated satisfy the governing equations. Even though Gaussian Process model uncertainty and can be used to generate samples from



1148
1149
1150
1151
1152
1153
1154
1155
1156
1157
1158
1159
1160
1161
1162
1163
1164
1165
1166
1167
1168
1169
1170
1171
1172
1173
1174
1175
1176
1177
1178
1179
1180
1181
1182
1183
1184
1185
1186
1187

Figure 7: Comparison of generated samples by physics-informed PDEDEIFF and PINN for unit circle. The dotted red line shows the ground truth and the blue dots are the inference point clouds.

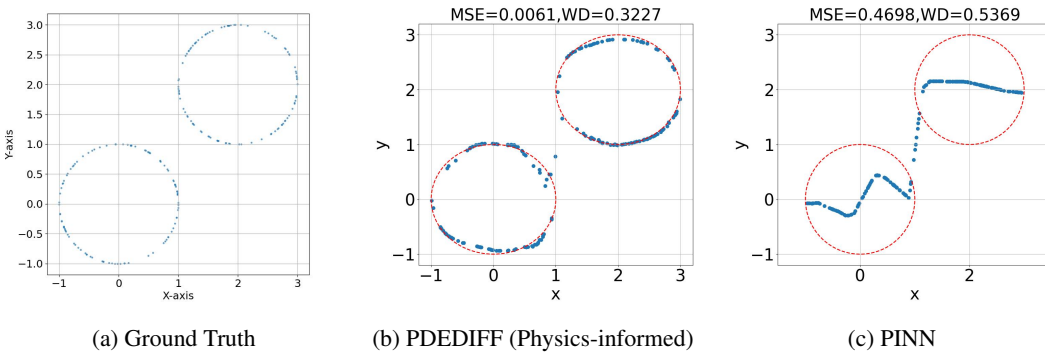


Figure 8: Comparison of generated samples by physics-informed PDEDEIFF and PINN for disjoint circles. The dotted red line shows the ground truth and the blue dots are the inference point clouds.

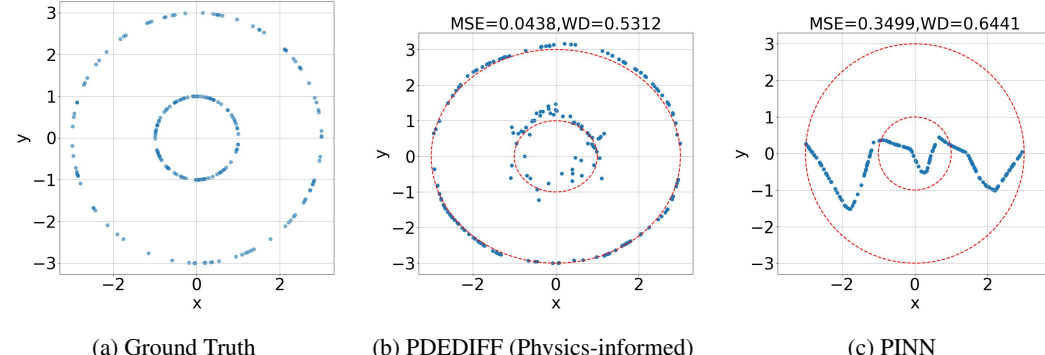
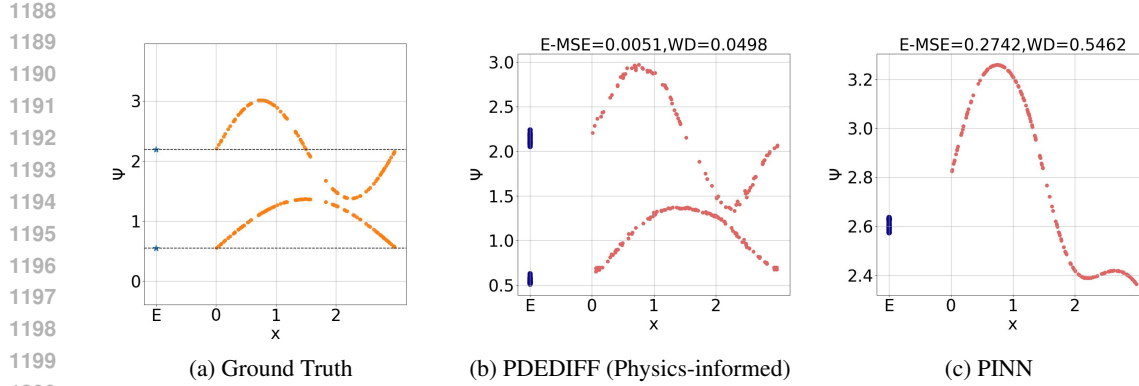


Figure 9: Comparison of generated samples by physics-informed PDEDEIFF and PINN for concentric circles. The dotted red line shows the ground truth and the blue dots are the inference point clouds.



1201 Figure 10: Comparison of generated samples by physics-informed PDEDIFF and PINN for 1D
1202 Schrödinger equation with 2 wavefunctions in infinite potential well.

1203
1204
1205 the solution like diffusion models, the inherent Gaussian assumption implies a unimodal function,
1206 and hence the goal of this approach is still to learn the mean function. As a result, Gaussian Process
1207 based methods cannot handle settings where the PDEs have multiple feasible solutions.

1208
1209
1210
1211
1212
1213
1214
1215 We compare PDEDIFF with the EPGP method in Harkonen et al. (2023) on solving the 1D
1216 Schrödinger equation for infinite potential well with 2 states. For the Gaussian Process models,
1217 because our data has samples from multiple solutions, we address this information to the kernel by
1218 adding two RBF kernels, or multiplying 2 RBF kernels and we observe that the model is trying to
1219 fit itself onto both the possible solutions. Whereas, we follow the method in Harkonen et al. (2023)
1220 to write a physics-informed kernel and gave the additional information to use $n = 1, 2$ states. We
1221 again experiment with sum and product of these EPGP kernels. As observed in all the 4 cases in
1222 Figure 11, Gaussian Process kernels fail to learn to sample from multiple solutions.

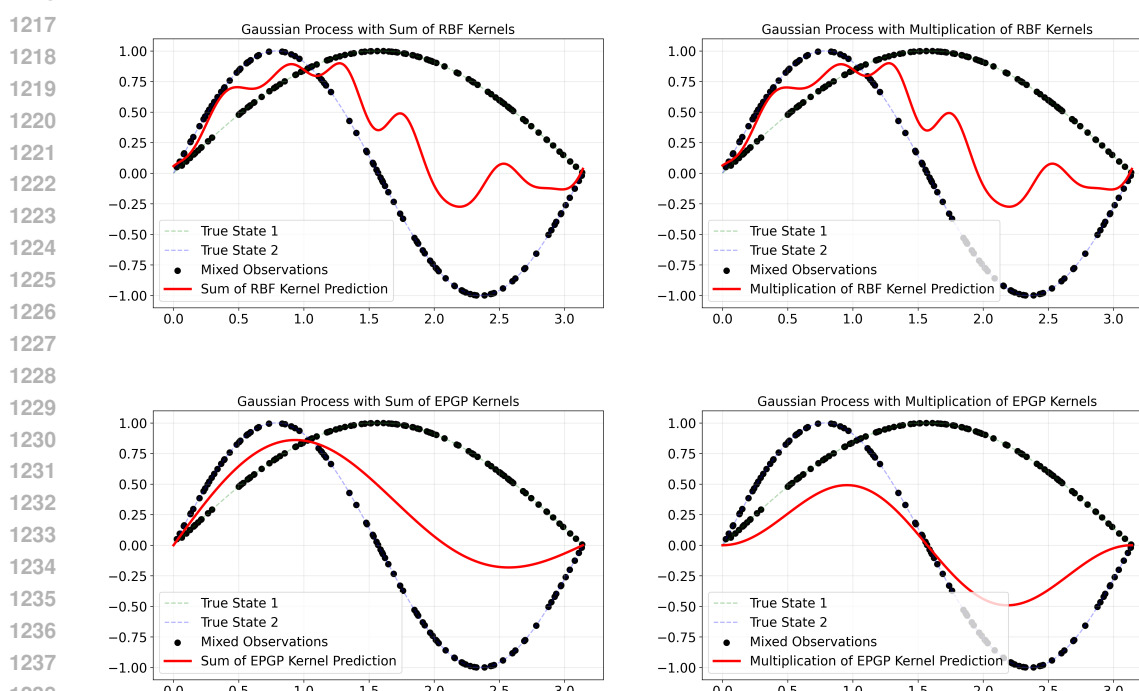


Figure 11: Gaussian Process Experiments for 1D Infinite Potential Well for $n = 1, 2$ eigenstates

1242 A.7 LIMITATIONS AND FUTURE WORK
1243

1244 As briefly discussed in the main paper, we have demonstrated that PDDEIFF provides a more flexible
1245 approach towards incorporating physics in diffusion models as the data is no longer bound to a mesh
1246 and the calculation of physics residual can be performed using autograd instead of writing custom
1247 finite difference kernels. We have also presented evidence that adding a physics informed loss to a
1248 conditional diffusion model can generate solution of PDEs that are more faithful to the underlying
1249 physics as compared to using a PINN or a vanilla diffusion model.

1250 Our method lays the foundation for many possible extensions, such as developing a training algo-
1251 rithm to train the diffusion model to learn unseen eigenstates when a particular subset of eigenstates
1252 have been provided for training. Another possible future extension could be to develop a data-free
1253 approach where no dataset will be required and the denoising step can be guided to generate solu-
1254 tions using the physics informed regularizer.

1255 In a preliminary experiment, we compare the time taken to solve first 4 eigenvalues and eigenfunc-
1256 tions for the 2D infinite potential well Schrodinger equation using an eigensolver (SciPy) on a
1257 1000×1000 grid with the time taken to sample 10^6 samples from the same grid using PDDEIFF.
1258 The eigensolver took almost 5708 seconds whereas PDDEIFF took only around 3126 seconds which
1259 is a 1.8 times faster. A potential research direction would be to speed-up the training and sampling
1260 time as this could help make the existing PDDEIFF sampler more efficient to generate data on new
1261 spatial-temporal coordinates.

1262 Previously, we had also mentioned that scaling this framework to noisy and high-dimensional ex-
1263 perimental datasets could potentially accelerate the development of real-time digital simulations of
1264 various problems. We believe that our method could be extended to other fields such as to drug
1265 discoveries, healthcare and finance, where systems can be modeled as PDEs and these PDEs will
1266 have multiple solutions.

1267 A.8 ABLATION STUDY
1268

1269 To study which weight c_{res} would be best guided our physics-informed PDDEIFF, for each setting,
1270 we ran 5 experiments for each value $c_{res} \in \{0, 0.001, 0.005, 0.01, 0.05, 0.1, 1, 10\}$ and average
1271 the P-MSE and WD metrics. The best average metrics for non-zero c_{res} for each setting of the
1272 Schrodinger equations, and non-homogeneous Helmholtz equation are presented in Table 1 and
1273 Table 2 of the main paper.

1274 A.8.1 ON WEIGHTS FOR RESIDUAL LOSS AND METRICS
1275

1276 In the circle experiments, where the ground truth distribution $\mathbb{P}(Y|X)$ has finitely many modes,
1277 PDDEIFF successfully captures all branches of the distribution. PINN, however, treats the problem
1278 as a regression task, learning the conditional mean $\mathbb{E}(Y|X)$ and thus fails to accurately predict the
1279 y -values for given x -coordinates. More visualizations of our toy examples that demonstrate this
1280 behavior can be found in 9, 8, 7.

1281 As we increase the c_{res} value for the physics constraint, this reduces our training loss as well as the
1282 PMSE metric (results shown in Table 5, 6, 7, 8, 9 and better illustrated in Figure 14, 15). Small
1283 c_{res} values (0.001, 0.005, 0.01) give low P-MSE and WD metric, with $c_{res} = 0.001$ achieving the
1284 best P-MSE and WD for learning 3 wavefunctions for 1D TISE, and $c_{res} = 0.005$ achieving the
1285 best metrics for learning 2 wavefunctions for 1D TISE and 1D GP, as shown in Table 5, 7, and 6,
1286 respectively. An example of the learned denoising process with $c_{res} = 0.001$ is shown in figure 5.

1287 For 1D Schrodinger cases, a higher c_{res} , i.e. $c_{res} = 0.1, 1, 10$ resulted in a flatter curve distribution
1288 (figure 13) compared to the distribution learned with a smaller $c_{res} = 0.001, 0.005, 0.01$ (figure
1289 12). One reason might be that strong physics residuals make the distribution converge to the trivial
1290 solution where the wavefunction $\psi(x) = 0$ and the energy $E = 0$. This trivial solution also satisfies
1291 the Schrodinger equation of the form $\mathcal{H}\psi = E\psi$. In addition, more points tend to concentrate around
1292 the first predicted eigenvalue, or also known as mode collapsed. This occurs when we enforce a
1293 strong penalty on the physics-informed loss.

1294 Across all settings, the residual weight (c_{res}) is balancing the two scenarios: a small value allows
1295 for more flexible generation, while for larger values it forces the model to learn a trivial solution. As

c_{res}	Setting	Unit circle		Disjoint circles		Concentric circles	
		P	Q	P	Q	P	Q
0	MSE	0.389±0.058	0.0028±0.0014	0.489±0.053	0.013±0.0023	0.277±0.085	0.052±0.014
	WD	0.475±0.010	0.0116±0.0192	0.533±0.015	0.421±0.055	0.907±0.032	0.560±0.038
0.01	MSE	0.379±0.085	0.0014±0.0006	0.486±0.052	0.012±0.0038	0.274±0.092	0.052±0.012
	WD	0.471±0.013	0.0852±0.0191	0.532±0.015	0.417±0.089	0.906±0.037	0.549±0.030

Table 4: Performance comparison between PINN (P) and PDEDEIFF (Q) across different problem settings. Here, MSE is as defined in section A.4.1 and WD is the Wasserstein metric for uniform distribution on circles defined in section A.4.2. The error is range of one standard deviation.

observed in Table 5, 6, and 7, increasing c_{res} , causes the model to collapse to a single mode, [where the PMSE remains small for PDEDEIFF, but the Wasserstein distance increases](#).

Similarly, for the 2D Schrodinger cases, we can see a similar trend with respect to c_{res} in Table 8, 9. For the harder 4 wave case, PDEDEIFF achieves a better Wasserstein metric as compared to the other methods. Since the "average" eigenstate for the 4 waves is the degenerate state, i.e., the eigenstates with the same energy ((1, 2), (2, 1)), PINN is able to give a much lower P-MSE value, but we can see from the Wasserstein metric, the samples generated have collapsed onto this average state and is not able to generate a mixture of all the learned states. PDEDEIFF in this case is still able to prevent this catastrophic mode collapse and generate a good mixture of eigenstates.

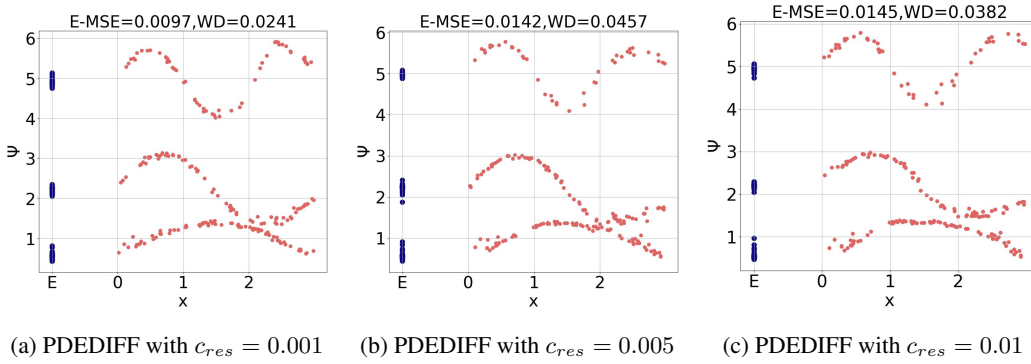


Figure 12: Generated samples by physics-informed PDEDEIFF with different c_{res} values for 1D Schrodinger equation in infinite potential well.

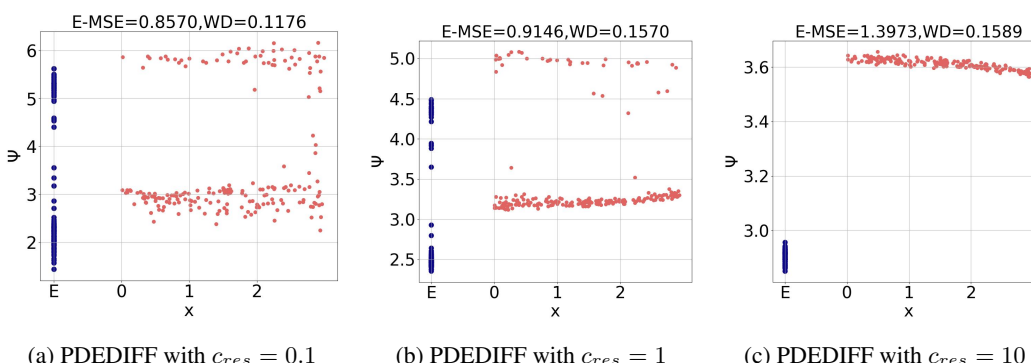


Figure 13: Generated samples by physics-informed PDEDEIFF with different c_{res} values for 1D Schrodinger equation in infinite potential well.

1350

1351

1352

1353

1354

1355

1356

1357

1358

1359

1360

1361

1362

1363

1364

1365

1366

1367

1368

1369

1370

1371

1372

1373

Table 5: Performance comparison between PINN (P), DeepONet (D), Physic-informed Neural Operator (N), and PDEDIFF (Q) for 1D (2 waves).

1374

1375

1376

1377

1378

1379

1380

1381

1382

1383

1384

1385

1386

1387

1388

1389

1390

1391

1392

1393

1394

1395

1396

1397

1398

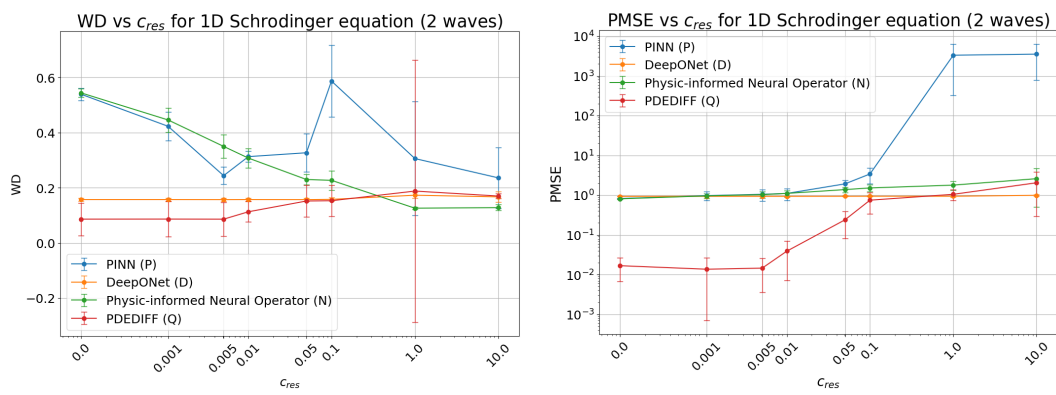
1399

1400

1401

1402

1403

Figure 14: Ablation study results from Table 5 with error bar for 1D Schrodinger equation (2 waves). PDEDIFF achieves lowest PMSE and WD metric compare with PINN, Physics-informed Neural Operator and DeepONet for $c_{res} \leq 0.1$ values. Overall, PDEDIFF with $c_{res} = 0.005$ gives the lowest PMSE and WD metrics.

c_{res}	1D (3 waves: $n = 1, 2, 3$)				
	P	D	N	Q	
0	PMSE	0.371 ± 0.031	4.37 ± 0.029	0.3330 ± 0.0337	0.0218 ± 0.013
	WD	0.737 ± 0.023	0.114 ± 0.00275	0.7760 ± 0.0331	0.0549 ± 0.009
0.001	PMSE	0.460 ± 0.435	4.37 ± 0.029	0.4450 ± 0.0349	0.0123 ± 0.012
	WD	0.422 ± 0.151	0.114 ± 0.00275	0.4700 ± 0.1350	0.0499 ± 0.019
0.005	PMSE	0.521 ± 0.079	4.37 ± 0.029	0.5250 ± 0.0374	0.0299 ± 0.011
	WD	0.315 ± 0.088	0.114 ± 0.00275	0.3370 ± 0.0827	0.0716 ± 0.014
0.01	PMSE	0.534 ± 0.167	4.37 ± 0.029	0.5831 ± 0.0449	0.0347 ± 0.006
	WD	0.266 ± 0.064	0.114 ± 0.00275	0.2907 ± 0.0643	0.0838 ± 0.022
0.05	PMSE	1.330 ± 0.528	4.38 ± 0.0307	0.8140 ± 0.0964	0.532 ± 0.222
	WD	0.399 ± 0.154	0.114 ± 0.00287	0.1920 ± 0.0316	0.176 ± 0.130
0.1	PMSE	7.63 ± 6.148	4.38 ± 0.0335	0.9540 ± 0.1395	0.807 ± 0.108
	WD	0.503 ± 0.132	0.115 ± 0.00327	0.1270 ± 0.0045	0.111 ± 0.013
1	PMSE	6989 ± 6330	4.41 ± 0.0335	1.0800 ± 0.1151	0.971 ± 0.171
	WD	0.224 ± 0.149	0.113 ± 0.00676	0.1320 ± 0.0251	0.145 ± 0.059
10	PMSE	7552 ± 5669	4.20 ± 0.138	2.1200 ± 2.5231	1.56 ± 1.61
	WD	0.154 ± 0.056	0.165 ± 0.0621	0.1260 ± 0.0161	0.143 ± 0.0241

Table 6: Performance comparison between PINN (P), DeepONet (D), Physic-informed Neural Operator (N), and PDEDIFF (Q) for 1D (3 waves).

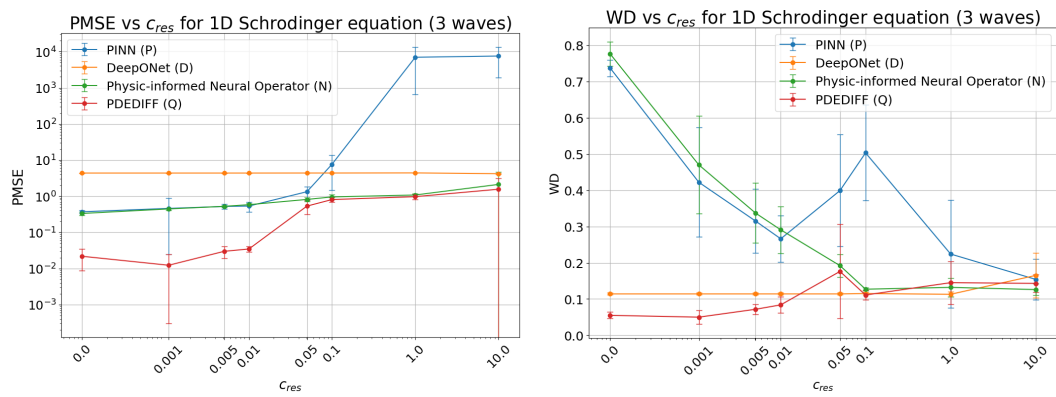


Figure 15: Ablation study results from Table 6 with error bar for 1D Schrodinger equation (3 waves). PDEDIFF achieves lowest PMSE and WD metric compare with PINN, Physics-informed Neural Operator and DeepONet for small c_{res} values. Overall, PDEDIFF with $c_{res} = 0.001$ gives the lowest PMSE and WD metrics.

1458

1459

1460

1461

1462

1463

1464

1465

1466

1467

1468

1469

1470

1471

1472

1473

1474

1475

1476

1477

1478

1479

1480

1481

1482

1483

1484

1485

1486

1487

1488

1489

1490

1491

1492

1493

1494

1495

1496

1497

1498

1499

1500

1501

1502

1503

1504

1505

1506

1507

1508

1509

1510

1511

Setting		1D GP (3 waves: $n = 1, 2, 3$)			
c_{res}		P	D	N	Q
0	PMSE	1.550 \pm 0.804	0.868 \pm 0.004	0.0685 \pm 0.00263	0.140 \pm 0.007
	WD	2.036 \pm 1.222	1.431 \pm 0.027	1.180 \pm 0.0449	0.195 \pm 0.043
0.001	PMSE	1.291 \pm 0.479	0.867 \pm 0.00487	0.0691 \pm 0.00260	0.126 \pm 0.019
	WD	2.418 \pm 1.084	1.431 \pm 0.0274	1.185 \pm 0.0451	0.194 \pm 0.033
0.005	PMSE	1.550 \pm 0.804	0.868 \pm 0.00451	0.0708 \pm 0.00243	0.118 \pm 0.028
	WD	2.040 \pm 1.222	1.430 \pm 0.0274	1.203 \pm 0.0472	0.338 \pm 0.186
0.01	PMSE	1.550 \pm 0.804	0.868 \pm 0.00438	0.0732 \pm 0.00222	0.139 \pm 0.032
	WD	2.036 \pm 1.222	1.431 \pm 0.0274	1.223 \pm 0.0533	0.333 \pm 0.187
0.05	PMSE	1.550 \pm 0.804	0.869 \pm 0.00440	0.0874 \pm 0.00399	0.134 \pm 0.018
	WD	2.040 \pm 1.222	1.430 \pm 0.0276	1.236 \pm 0.0903	0.937 \pm 0.734
0.1	PMSE	1.550 \pm 0.804	0.871 \pm 0.00507	0.0930 \pm 0.00923	0.189 \pm 0.089
	WD	2.040 \pm 1.222	1.430 \pm 0.0276	1.144 \pm 0.175	0.644 \pm 0.453
1	PMSE	1.550 \pm 0.804	0.898 \pm 0.00864	0.1016 \pm 0.00198	0.248 \pm 0.137
	WD	2.040 \pm 1.222	1.430 \pm 0.0260	1.899 \pm 0.889	1.100 \pm 0.565
10	PMSE	1.550 \pm 0.804	0.915 \pm 0.0427	0.1016 \pm 0.00197	0.286 \pm 0.204
	WD	2.040 \pm 1.222	1.120 \pm 0.0841	2.992 \pm 0.414	0.453 \pm 0.072

Table 7: Performance comparison between PINN (P), DeepONet (D), Physic-informed Neural Operator (N), and PDDEIFF (Q) for the 1D GP (3 waves) setting. Lower values indicate better agreement with the ground truth wavefunctions.

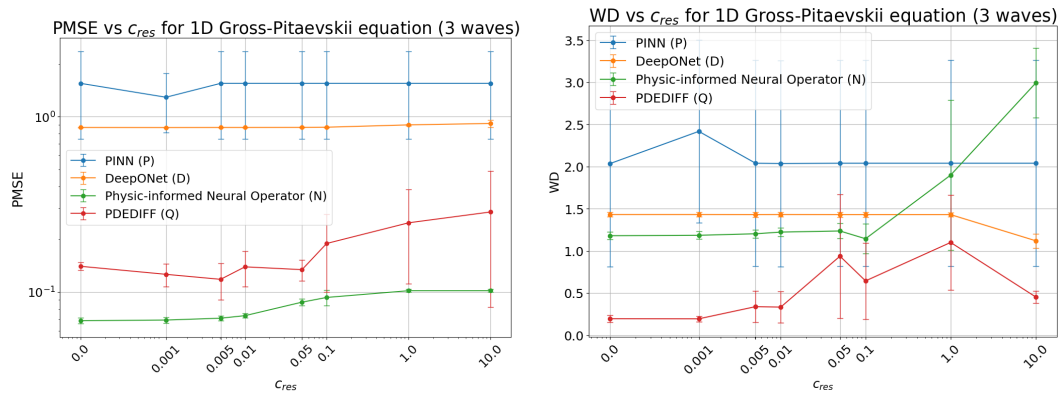


Figure 16: **Ablation study results from Table 7 with error bar for 1D Gross-Pitaevskii equation (3 waves).** PDDEIFF achieves lowest WD metric compare with PINN, Physics-informed Neural Operator and DeepONet for all $c_{res} \leq 10$ values. Physics-informed neural operator converges to a single mode to achieve the small PMSE metric but failed to learn the whole multi-modal distribution with all 3 wavefunctions. This showed in Figure 4 and the high WD metric.

1512

1513

1514

1515

1516

1517

1518

1519

1520

1521

1522

1523

1524

1525

1526

1527

1528

1529

1530

1531

1532

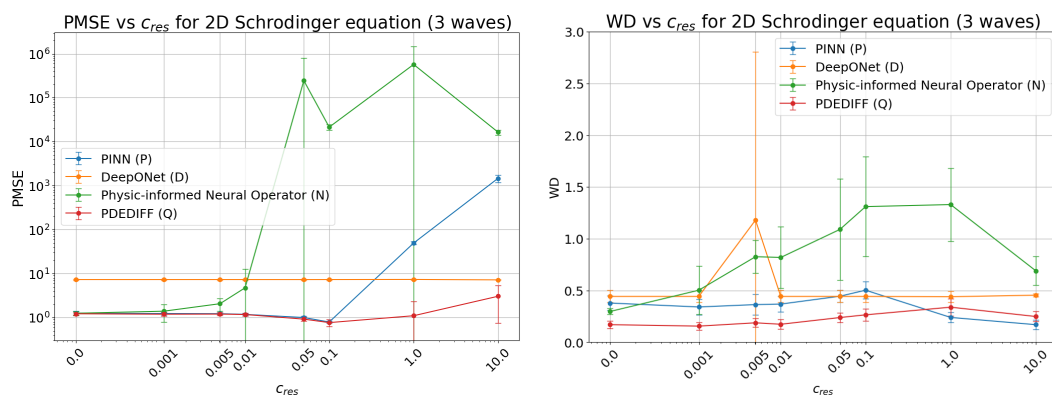
1533

1534

1535

1536

Table 8: Results for the 2D (3 waves: (1, 1), (2, 1), (2, 2)) experiment, comparing PINN (P), DeepONet (D), Neural Operator (N), and PDDEIFF (Q).

Figure 17: Ablation study results from Table 8 with error bar for 2D Schrodinger equation (3 waves). PDDEIFF achieves lowest WD and PMSE metric compare with PINN, Physics-informed Neural Operator and DeepONet for all $c_{res} \leq 0.1$ values. PDDEIFF with $c_{res} = 0.1$ gives the lowest PMSE metric and PDDEIFF with $c_{res} = 0.001$ gives the lowest WD metric.

1563

1564

1565

1566

1567

1568

1569

1570

1571

1572

1573

1574

1575

1576

1577

1578

1579

1580

1581

1582

1583

1584

1585

1586

1587

1588

1589

1590

Table 9: Results for 2D (4 waves: (1, 1), (1, 2), (2, 1), (2, 2)) experiment, comparing PINN (P), DeepONet (D), Neural Operator (N), and PDDEIFF (Q).

1591

1592

1593

1594

1595

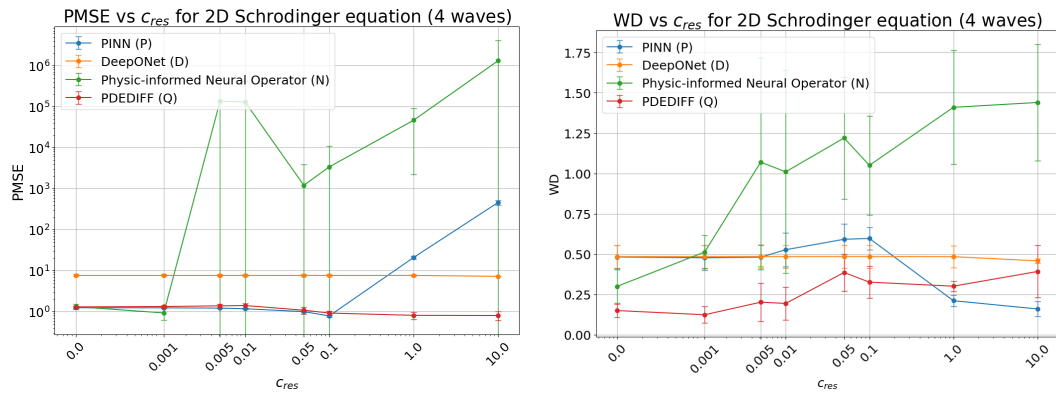
1596

1597

1598

1599

1600

Figure 18: Ablation study results from Table 9 with error bar for 2D Schrodinger equation (4 waves). PDDEIFF achieves lowest WD metric compare with PINN, Physics-informed Neural Operator and DeepONet for all $c_{res} \leq 0.1$ values. PINN with $c_{res} = 10$ gives the lowest PMSE metric and PDDEIFF with $c_{res} = 0.001$ gives the lowest WD metric.

1610

1611

1612

1613

1614

1615

1616

1617

1618

1619

1620

1621

1622

1623

1624

1625

1626

Setting		2D (4 waves: (1, 1), (2, 1), (3, 1), (4, 1))			
c_{res}		P	D	N	Q
0	PMSE	1.1333 \pm 0.0696	22.342 \pm 2.3903	1.1984 \pm 0.1170	1.1004 \pm 0.0490
	WD	0.5973 \pm 0.1604	0.5127 \pm 0.1082	0.3442 \pm 0.1107	0.22174 \pm 0.1484
0.001	PMSE	1.1299 \pm 0.05626	22.342 \pm 2.3903	1.2570 \pm 0.5490	1.0905 \pm 0.0559
	WD	0.6233 \pm 0.0560	0.5127 \pm 0.1082	0.58746 \pm 0.1358	0.20494 \pm 0.0891
0.005	PMSE	1.9343 \pm 0.7272	22.342 \pm 2.39033	2.2754 \pm 2.1479	1.0326 \pm 0.1810
	WD	0.4815 \pm 0.0074	0.5128 \pm 0.1083	0.67119 \pm 0.2896	0.38876 \pm 0.2228
0.01	PMSE	1.6699 \pm 0.8890	22.342 \pm 2.3903	8328.97 \pm 18620	0.9246 \pm 0.1270
	WD	0.4702 \pm 0.0269	0.5127 \pm 0.1082	0.8739 \pm 0.5174	0.5585 \pm 0.1533
0.05	PMSE	2.0404 \pm 1.3113	22.344 \pm 2.3907	1774100 \pm 3922300	0.7339 \pm 0.1237
	WD	0.46002 \pm 0.0199	0.51276 \pm 0.1082	1.1972 \pm 0.4778	0.4753 \pm 0.0588
0.1	PMSE	2.2239 \pm 1.5007	22.350 \pm 2.3901	604850 \pm 1335200	0.6149 \pm 0.1649
	WD	0.4576 \pm 0.0203	0.5127 \pm 0.1081	1.3754 \pm 0.5193	0.4431 \pm 0.0244
1	PMSE	15.223 \pm 16.508	22.362 \pm 2.2990	31462.9 \pm 69532.2	1.50 \pm 2.2162
	WD	0.5161 \pm 0.0757	0.5129 \pm 0.1050	1.0066 \pm 0.3278	0.4436 \pm 0.0018
10	PMSE	637.61 \pm 197.99	20.565 \pm 0.5769	863.57 \pm 375.39	4.3467 \pm 8.2002
	WD	0.6188 \pm 0.1821	0.4660 \pm 0.0136	0.7310 \pm 0.0744	0.4640 \pm 0.0443

Table 10: Results for the 2D (4 waves: (1, 1), (2, 1), (3, 1), (4, 1)) experiment, comparing PINN (P), DeepONet (D), Neural Operator (N), and PDDEIFF (Q).

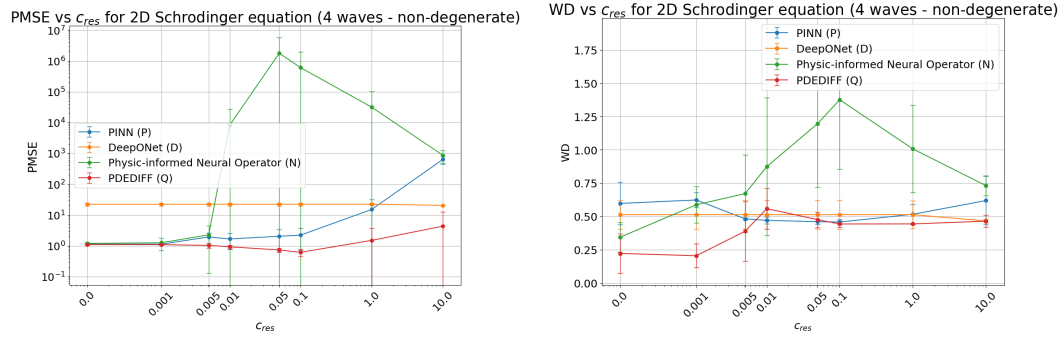


Figure 19: Ablation study results from Table 10 with error bar for 2D Schrödinger equation (4 waves). PDDEIFF achieves lowest PMSE metric compare with PINN, Physics-informed Neural Operator and DeepONet for all c_{res} values. PDDEIFF with $c_{res} = 0.001$ gives the lowest WD metric.

Setting		Helmholtz (2 parameters: $k \in \{\pi, 4\pi\}$)			
c_{res}		P	D	N	Q
0	PMSE	0.800 ± 0.110	21.35 ± 2.67	0.753 ± 0.217	0.254 ± 0.153
	WD	0.107 ± 0.0401	0.168 ± 0.00103	0.111 ± 0.0425	0.0915 ± 0.0052
0.001	PMSE	0.746 ± 0.315	21.35 ± 2.67	1.00 ± 1.62	0.227 ± 0.0867
	WD	0.108 ± 0.0297	0.168 ± 0.00103	0.106 ± 0.0463	0.0913 ± 0.00615
0.005	PMSE	0.918 ± 0.164	21.4 ± 2.67	99.5 ± 178.81	0.320 ± 0.133
	WD	0.102 ± 0.00921	0.168 ± 0.00103	0.303 ± 0.153	0.0874 ± 0.00455
0.01	PMSE	1.18 ± 0.476	21.35 ± 2.67	0.909 ± 1.01	0.570 ± 0.187
	WD	0.109 ± 0.0234	0.168 ± 0.00103	0.160 ± 0.148	0.0886 ± 0.00580
0.05	PMSE	38.4 ± 17.41	21.6 ± 2.76	140 ± 126.08	2.740 ± 2.170
	WD	0.0866 ± 0.00753	0.168 ± 0.001034	0.0925 ± 0.0121	0.0819 ± 0.00715
0.1	PMSE	48.7 ± 19.58	23.4 ± 3.02	159 ± 145.52	4.430 ± 0.566
	WD	0.0875 ± 0.00734	0.167 ± 0.001047	0.0937 ± 0.0126	0.0803 ± 0.00419
1	PMSE	74.6 ± 27.11	11.1 ± 9.56	196 ± 158.64	5.510 ± 0.581
	WD	0.0888 ± 0.00670	0.173 ± 0.03096	0.0987 ± 0.0134	0.0827 ± 0.00703
10	PMSE	89.9 ± 25.42	0.557 ± 0.000874	458 ± 246.35	6.540 ± 1.234
	WD	0.0901 ± 0.00637	0.158 ± 0.0280	0.169 ± 0.0566	0.0746 ± 0.00446

Table 11: Results for the Helmholtz (2 parameters) experiment, comparing PINN (P), DeepONet (D), Physics-informed Neural Operator (N), and PDEDIFF (Q).

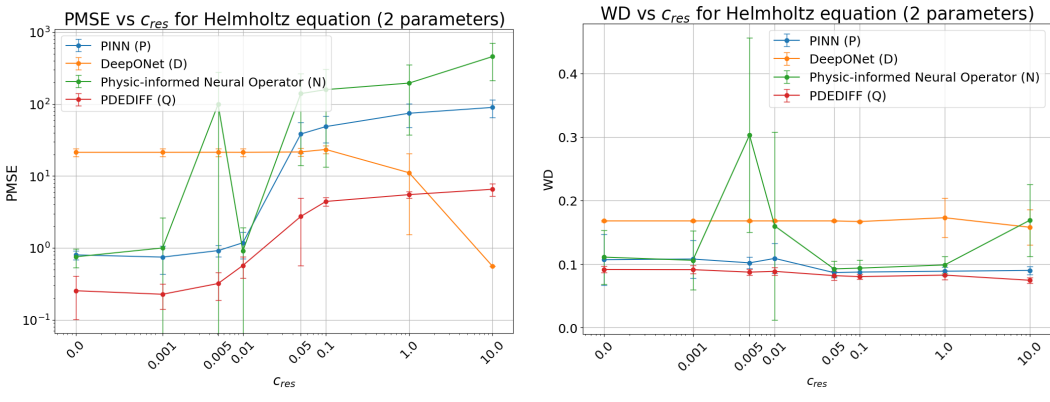


Figure 20: Ablation study results from Table 11 with error bar for Helmholtz equation (4 waves). PDEDIFF achieves lowest PMSE metric compare with PINN, Physics-informed Neural Operator and DeepONet for all $c_{res} \leq 1$ values. PDEDIFF with $c_{res} = 0.001$ gives the lowest PMSE metric and PDEDIFF with $c_{res} = 10$ gives the lowest WD metric.